Chemical Engineering Journal 494 (2024) 152843

Contents lists available at ScienceDirect

Chemical Engineering Journal

journal homepage: www.elsevier.com/locate/cej

Synergistic effect of graphitic-like carbon nitride and sulfur-based thiazole-linked organic polymer heterostructures for boosting the photocatalytic degradation of pharmaceuticals in water

Raziyeh Zandipak [a,c,*], Nader Bahramifar [a], Morteza Torabi [b], Mónica Calero [c], Mario J. Muñoz-Batista [c], Rafael R. Solís [c,*]

[a] Department of Environmental Science, Faculty of Natural Resources and Marine Sciences, Tarbiat Modares University, Noor, Iran
[b] Department of Organic Chemistry, Faculty of Chemistry and Petroleum Sciences, Bu-Ali Sina University, Hamedan, Iran
[c] Department of Chemical Engineering, Faculty of Sciences, University of Granada, Avda. Fuentenueva, 18014 Granada, Spain

ARTICLE INFO

Keywords:
Covalent Organic Framework
Graphitic Carbon Nitride
Microwaved-assisted synthesis
Photocatalysis
Water Treatment

ABSTRACT

A sulfur-based COF has been combined with graphitic carbon nitride (CN) in microwave-assisted synthesis to build a COF-CN heterostructure with enhanced photocatalytic activity. The prepared COF-CN heterostructures were fully characterized, analyzing the textural (N_2 isotherms), structural (XRD and FTIR), chemical (elemental analysis and XPS), morphological (HR-STEM), optical (DRS-UV–Vis and photoluminescence) and electrochemical properties (EIS impedance, transient photocurrent, and flat band potential). Different COF-to-CN ratios (5–25 % of COF, wt.) were explored, defining a proportion (20 %) that led to optimum activity for the photocatalytic oxidation of organic contaminants of emerging concern (CECs) due to an enhanced separation of the photogenerated charges and lower bandgap value, 2.55 vs. 2.35 eV. The performance of the optimum COF-CN was further tested for other CECs, demonstrating its benefits compared to the bare CN. The materials displayed acceptable reusability and stability. The activation mechanism highlights the importance played by superoxide radicals and photogenerated holes.

1. Introduction

Photocatalysis is a promising sustainable alternative to large-scale solar energy storage. Under convenient irradiation, a semiconductor can transform the absorbed photons into energy delivered to drive reactions that, if not thermodynamically impeded, the reaction rate under darkness is sparse [1]. The research of photocatalysis has skyrocketed during the last decades, exploring diverse applications such as the oxidation of aqueous pollutants either of inorganic or organic origin [2], water splitting [3], CO_2 photoreduction [1,4], N_2 fixation [5,6], or the selective synthesis of organic molecules with interest in the industry [7–10]. Among the abundant metallic semiconductors, in which TiO_2 outstands in almost all applications, the polymeric non-metallic graphitic-like carbon nitride has recently attracted attention due to its easy preparation from natural resources such as urea or easily synthesized as melamine. The bandgap of g-C_3N_4 is lower than the benchmark TiO_2, 2.7 vs 3.2 eV [11], which allows a better harvesting of the solar spectrum. However, like most photocatalysts, g-C_3N_4 lacks an efficient separation of charges that minimizes the undesirable recombination effect. To overcome this limitation, g-C_3N_4 has been modified, modifying the surface properties by the insertion of oxygenated groups [12], via non-metal doping [13–16], or combining it with other semiconductors to build a heterojunction [17–20].

The development of solids based on metal-organic frameworks (MOFs) [21,22] and covalent organic frameworks (COFs) [23–25] with photocatalytic properties, including solar light harvesting, has skyrocketed in the last years. Both are of paramount interest in the development of novel materials due to their textural properties, morphology at the nanoscale, and electronic properties, all of them easily tunable by a proper design of the scaffolding blocks and the synthesis at a molecular level. Compared to COFs, MOFs display much more morphologies due to the higher possibilities of multiple coordination around the metal cluster [26]. Nonetheless, COFs, built exclusively from covalent binding, lead to robust linkages that enable them to be stable in the presence of water avoiding hydrolysis [27], a recurrent drawback in most MOFs [28,29]. The high stability towards aqueous environments is due to the high

* Corresponding authors.
E-mail addresses: r.zandipak@modares.ac.ir (R. Zandipak), rafarsolis@ugr.es (R.R. Solís).

https://doi.org/10.1016/j.cej.2024.152843
Received 1 March 2024; Received in revised form 1 June 2024; Accepted 3 June 2024
Available online 4 June 2024

hydrophobicity of COFs [30]. Among all the plausible COFs being under research, covalent triazine framework polymers, prepared by the aromatic 1,3,5-triazine rings, were set up in 2008 [31] and have acquired utmost importance due to the high chemical stability of the frameworks conjugated structure prepared from this unit. Moreover, the COFs based on triazine are sensitive to radiation and display properties as semiconductors [32]. The condensation of tri(4-formylphenoxy) cyanurate (TFPC) via dynamic nucleophilic aromatic substitution has been reported recently, obtaining a tacked planar material with good stability and high CO_2 adsorption capacity [33]. COF bearing a π-electron deficient triazine core and a π-electron rich core containing phenyl and naphthalene rings connected with –O and –N donor Lewis basic sites in hexagonal honeycomb layers has been reported from the imine reaction of TFPC and naphthalene diamino [34].

This work reports a sulfur-based COF made from the polycondensation of TFPC and naphthalene diamine. The resultant COF displayed visible radiation absorption, i.e. greenish appearance, but was highly hydrophobic. To overcome the hydrophobic drawback, COFs are commonly modified, joining them to other semiconductors with favorable surface interaction with water [35]. For that reason, the resulting COF was combined with graphitic-carbon nitride, a metal-free polymeric semiconductor [11,36,37], in a microwave-assisted synthesis pot, considerably reducing the time of synthesis [38,39]. The prepared COF-CN heterostructure displayed enhanced photocatalytic properties for the degradation of contaminants of emerging concern in water.

2. Experimental section

2.1. Synthesis of COF and COF-CN heterostructures

2.1.1. Synthesis of the COF and graphitic-like carbon nitride (CN)

For the synthesis of the COF, firstly tri-(4-formylphenoxy) cyanurate (TFPC) was obtained from the reaction of cyanuric chloride with 4-hydroxybenzaldehyde. For that, 20 mmol of 4-hydroxybenzaldehyde and 20 mmol of NaOH were dissolved in 80 mL of deionized water. After, 4 mmol of cyanuric chloride, dissolved in 40 mL of acetone, was slowly dropwise added to the previous solution. The mixture was stirred at room temperature for 5 h to complete the reaction, leading to the formation of a white solid which was filtered and washed with ethanol and aqueous sodium bicarbonate solution.

The COF was prepared by adding 0.456 mmol of TFPC, 0.684 mmol of 1,5-diaminonaphthalene, 2 mmol of sulfur, 0.2 mL of dimethyl sulfoxide (DMSO), and 5 mL of dimethyl formamide (DMF). The resulting solution was submitted to thermal treatment under reflux at 140 °C for 24 h to promote the polymerization reaction, see Fig. 1**A**. The resulting greenish precipitate was washed several times with methanol, tetrahydrofuran, and trichloro-ethylene to remove the unreacted chemicals. The washed solid was dried under a vacuum at 80 °C overnight.

The graphitic-like carbon nitride sample (CN) was prepared by thermal polymerization of melamine at 550 °C for 1 h under an air atmosphere in a sealed crucible. The yellowish solid was treated with HCl 1 M (7 g/L of g-C_3N_4) to promote delamination under sonication and washed several times with water.

2.1.2. Synthesis of the COF-CN heterostructures

The COF-CN heterostructures were prepared by microwave-assisted solvothermal treatment, see a scheme of the synthesis route in Fig. 1**B**. For that, 1 g of CN and a defined amount of COF were placed in a Teflon line vessel with 25 mL of DMF. The vessel was sealed and magnetically stirred inside a high-pressure multimode flexiWAVE platform for microwave synthesis of Milestone®. The temperature was raised by the action of microwave radiation to 120 °C in 15 min and held at this value for 30 min. After, the samples were submitted to natural cooling. The resulting COF-CN heterostructures were washed several times with ultrapure water, and the recovered solid by centrifugation was dried overnight at 105 °C. The resulting samples were labeled as x%COF-CN were x (5–25) means the mass percentage of the COF placed in the synthesis procedure. For comparison purposes, the CN sample obtained by melamine polymerization was also submitted to microwave treatment following the same steps but lacking the addition of the COF.

2.2. Characterization of the COF-CN heterostructures

The crystallinity of the samples was studied by X-Ray Diffraction (XRD), in a Bruker D8 Discover (50 kV, 1 mA) diffractometer working with X-Ray from the Cu Kα (λ = 1.5406 Å) equipped with a Pilatus3R 100 K-A detector. The diffractograms were recorded at room temperature in the 2θ range of 4-70°, under a rate of 30 s per 0.02°. The software QualX® was used for the interpretation of the diffractograms and the determination of the crystal size through Scherrer's equation. The crystallite size was estimated by Scherrer's equation from the most intense peak and the interlayer spacing of the graphitic-like carbon nitride was estimated from the (002) peak. The relation $L_{crystal}/d_{layer}$ was used as an estimation of the number of layers of the graphitic-like structure [40].

The structural properties were also assessed by Fourier Transform InfraRed (FTIR) spectroscopy equipped with Attenuated Total Reflectance (ATR). The FTIR spectra were recorded in a Spectrum65 device

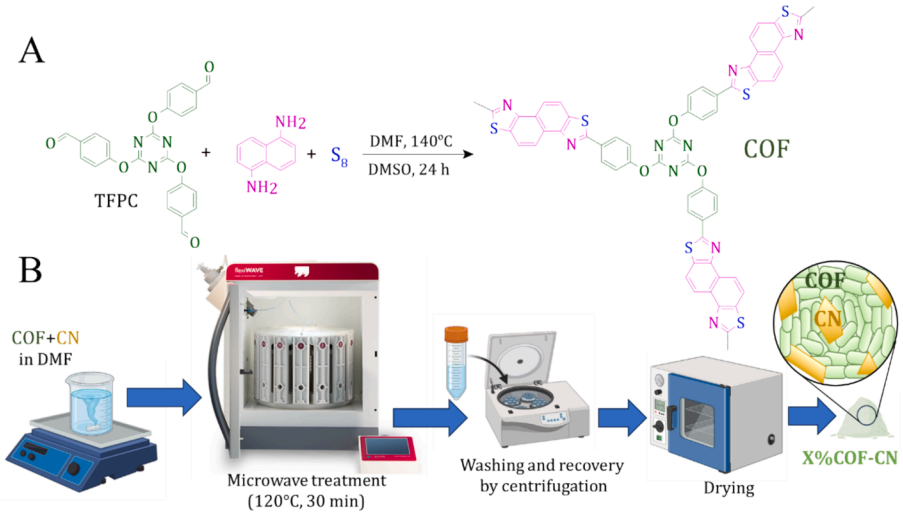

Fig. 1. Reaction scheme for the synthesis of the sulfur-based COF (A) and synthesis preparation of the COF-CN heterostructures by microwaved-assisted method (B).

from Perkin-Elmer®, monitoring the signal in the range 650–4000 cm^{-1}. The identification of the peaks with the plausible functional groups was carried out with the assistance of irAnalyze-RAManalyze software from LabCognition GmbH. In addition, Raman spectroscopy was conducted in a Micro-Raman Dispersive JASCO NRS-5100 spectrometer equipped with a diode laser of excitation of 785 nm (500 mW).

The textural properties were evaluated by N_2 physisorption. The N_2 adsorption–desorption isotherms at 77 K were obtained in a Sync 220 device of 3P Instruments®. The samples were previously degassed at 150 °C under vacuum overnight in a Prep J4 degasser station of 3P Instruments®.

The elemental composition was determined in a TrueSpec® Micro CHNS analyzer from Leco®. Moreover, the surface chemistry was analyzed by X-ray Photoelectron Spectroscopy (XPS) in a Kratos AXIS UltraDLD device equipped with an X-ray source from Al Kα. The spectra were referenced to adventitious C_{1s}, ascribed to 284.6 eV. The deconvolution of the spectra was conducted using the software XPSpeak 4.1®, applying a Shirley-type correction of the baseline background.

The morphology and element distribution of the COF-CN nanoparticles was observed by High-Resolution Scanning Transmission Electron Microscopy (HR-STEM) imaging in a Thermo Scientific™ Talos™ F200X (200 kV) equipped with High-Angle Annular Dark-Field imaging (HAADF) detector and Energy Dispersive X-Ray spectroscopy (EDX) microanalysis for the analysis of the composition and study of the element distribution.

The photoluminescence (PL) technique was conducted as an indirect measure of the recombination rate of the photogenerated electron-hole pair [41,42]. The analysis was conducted in a Varian Cary Eclipse fluorescence spectrometer, setting 365 nm as the excitation wavelength (slit 2.5 nm) and registering the emission spectra (slit 2.5 nm) from 400 to 600 nm.

The electrochemical characterization of the samples in terms of photocurrent, electrochemical impedance spectroscopy (EIS), Mott-Schottky analysis, and transient photocurrent tests, was carried out in a conventional three-electrode cell with 0.2 M Na_2SO_4 (pH = 7.0) as the electrolyte solution. The working electrode was prepared on indium-doped tin oxide (ITO) transparent conductive glass, a Pt wire and a saturated calomel electrode (SCE) were used as the counter and reference electrodes, respectively. The measurements were performed using a CHI 660C Electrochemical Workstation (USA).

2.3. Photocatalytic tests

The photocatalytic activity of the COF-CN heterostructures was assessed in the degradation of acetaminophen (ACE) in water. This contaminant was selected for a preliminary evaluation of the different COF-CN ratios based on its occurrence in different effluents including wastewater [43,44]. The photoreactor used was equipped with two UVA lamps of 9 W each emitting at a maximum wavelength of 365 nm. The lamps were placed in the inner space of a jacketed annular reactor made of borosilicate glass. The aqueous solution with the COF-CN sample was pumped to the inner space, magnetically stirred, from an auxiliary tank, also a stirrer, and equipped with refrigeration to maintain the temperature at 20 °C. Detailed information about the dimensions of the photoreactor can be checked in a previous work [19]. Air was bubbled into the auxiliary tank to ensure the saturation of O_2 in the aqueous solution. The photocatalytic experiments started feeding the system 350 mL of solution. The photocatalyst was next added to set a dose of 0.5 g L^{-1}. An adsorption period of 30 min in the absence of radiation, i.e. darkness, was carried out to ensure that the adsorption equilibrium was reached. Next, the lamps were switched on, and the evolution of the concentration of acetaminophen was monitored. The photocatalyst was removed by filtration with syringe filters (Millex PVDF, 0.45 μm). The photocatalytic tests involved experiments of degradation of acetaminophen at initially 5 mg L^{-1} for selecting the best performance. For further testing, the optimum photocatalyst was tested in the degradation of a mixture of compounds, i.e. a mixture of acetaminophen (ACE), caffeine (CAF), antipyrine (ANT), ciprofloxacin (CIP), sulfamethoxazole (SMX) and diclofenac (DCF), initially at 2 mg L^{-1} each. These compounds were considered based on their occurrence in wastewater [45]. Photolysis tests, i.e. absence of photocatalyst, were carried out for comparison purposes in both cases.

The concentration of acetaminophen was analyzed by high-pressure liquid chromatography (HPLC) in a Water Alliance e2695 HPLC device, equipped with a 2998 photodiode Array (PDA) detector. A Zorbax Bonus-RP column (5 μm, 4.6x150 mm) was used as the stationary phase. The mobile phase, pumped at a flow rate of 1 mL min^{-1} under the isocratic mode, was a mixture of acetonitrile (A) and ultrapure water acidified with 0.1 % (v/v) of trifluoroacetic acid (B). The analysis of ACE was carried out with an A: B mixture of 60:40 (vol.), and the quantification at 240 nm. For the analysis of the mixture, a gradient program was set up, starting with 5:95 pumped at 1 mL min^{-1} during 5 min, raising the acetonitrile proportion to reach 95:5 in 30 min and further kept at this proportion for 5 min. The quantification of ACE and ANT was conducted at 240 nm, CAF and SMX at 270 nm, DCF at 275 nm, and CIP at 280 nm.

The influence of pH in the range 3–9 on the photocatalytic activity of the most active sample was tested by adjusting the pH with NaOH or HCl 0.1 M. The effect of the presence of the most common inorganic anions on the photocatalytic performance of the most active sample was conducted by adding Cl^- (2.50 mM), NO_3^- (1 mM), or HCO_3^- (3 mM) at the maximum values in wastewater after reclamation treatment [46].

The role played by the different reactive oxidation species was assessed by tests in the presence of chemical scavengers, which were added to the solution before loading in the photoreactor. The role played by the superoxide radical was evaluated by replacing air with N_2, adding 1 mM p-benzoquinone (p-BZQ) or 1 mM disodium 4,5-dihydroxybenzene-1,3-disulfonate (tiron). 10 mM *tert*-butyl alcohol (TBA) was added to scavenge the contribution of hydroxyl radicals. The importance of the photogenerated holes was assessed by adding 10 mM oxalic acid. Moreover, the impact of $HO^\bullet$ was additionally assessed by an indirect probe method based on terephthalic acid (TPA) [47,48]. The non-fluorescent terephthalic acid traps $HO^\bullet$ triggering the formation of the fluorescent 2-hydroxy-terephthalic acid (2-HO-TPA) [49]. Thus, the monitoring of 2-HO-TPA formation can be considered as an indirect indicator of the $HO^\bullet$ presence in the aqueous solution. For this reason, a test with TPA 1 mM was carried out [50]. The analysis of 2-HO-TPA with the reaction time was conducted in a Varian Cary fluorescence spectrometer setting the excitation wavelength at 315 nm (slit 2.5 nm) and the emission spectra recorded between 360–600 nm (slit 2.5 nm), registering the maximum of the 2-HO-TPA spectrum peak at 420 nm. The correlation of the peak high with the concentration of the standard 2-HO-TPA was carried out in the range 0.5–5 μM, leading to a limit of detection of 0.21 μM.

3. Results and discussion

3.1. Characterization of the COF-CN heterostructures

The crystalline structure of the COF-CN heterostructures was analyzed by X-ray diffraction. Fig. 2**A** illustrates the diffractograms of the prepared materials. The diffractogram of the graphitic-like carbon nitride (CN) displayed diverse crystalline peaks, from which a sharp peak outstands the rest. The condensation of the precursor, i.e. melamine, triggers the formation of tris-s-triazine units which are polymerized in plates interacting by the π-π* interactions leading to a certain number of layers aggrupation [51,52]. Consequently, an intense peak located at roughly 27° is defined in CN materials, associated with the (0 0 2) diffraction plane defined by the interplanar aromatic interaction from π-π* interactions of the aromatic heptazine rings [53]. The polymerization conditions such as the temperature strongly impact the sharpness of this peak. The number of layers at condensation

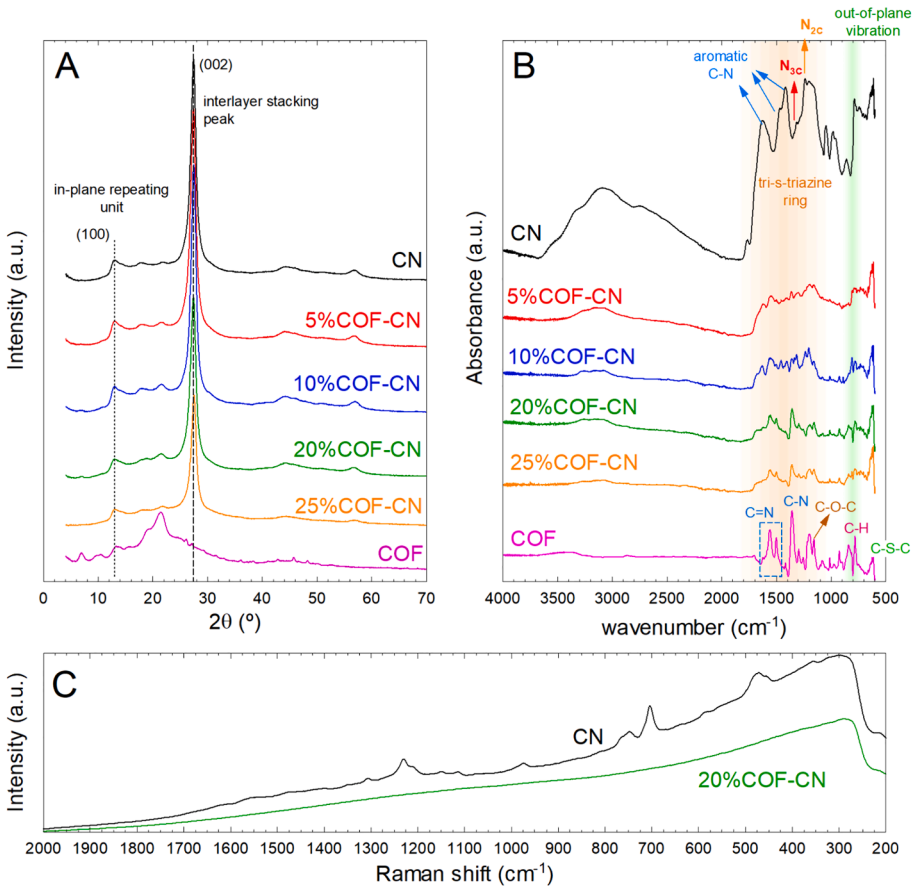

Fig. 2. XRD diffractograms (A), FTIR spectra (B), and Raman spectra (C) of the COF-CN heterostructures.

temperatures of 500 and 600 °C has been reported between approximately 22 and 31°, respectively [54]. A tentative estimation of the number the layers from the division of the crystal size and the d-spacing of the XRD interaction [40] suggested roughly 40 layers for the CN sample. The diffractogram of CN defines a second peak, much less intense and considerably broadened, placed at ca. 13°. This peak is attributed to the (1 0 0) plane, distinct from the intralayer spacing of the heptazine rings [55]. In the case of the COF, a much less intense diffraction pattern was obtained, which suggests the formation of a moderate crystalline polymer, which follows the already reported polymerization of TPFC and naphthalene diamino [34]. Similarly, a hexagonal staked layered structure with different ring widths due to sulfur incorporation is tentatively envisaged. The COF-CN structures defined a strong peak from the interlayer stacking of CN nanosheets, predominant from the COF XRD pattern due to the higher proportion and crystallinity of CN if compared to the COF. As reported in other g-C_3N_4 heterostructures, the modification of the material and the combination with other semiconductors alters the graphitic structure leading to less crystalline materials [56]. There was no observed tendency regarding the crystal size of the heterostructures, providing an estimation of the number of layers for the graphitic structure of 40–45.

The structural properties were analyzed by FTIR. The spectra depicted in Fig. 2**B** demonstrate important changes in their FTIR footprints. A broadband registered at 3000–3300 cm^{-1} appeared in CN due to the terminal N–H and O–H stretching, attributed to the primary amine (–NH_2) and adsorbed water molecules [42]. The decrease of the terminal groups may be associated with the interaction with the COF structure. The heating through microwave radiation assists in the creation of new bonds through a hot-spot mechanism [57]. Moreover, the interaction of COFs with 2D materials such as g-C_3N_4 takes place by π-π interactions [58] which seems not to be the case since a 2D COF cannot be surmised from the microscopy analysis. The vibration of the aromatic tri-s-triazine rings leads to different peaks. Thus, the vibration of secondary nitrogen (N_2C) and tertiary nitrogen (N_3C) define peaks located at 1225 and 1312 cm^{-1}, respectively [43]. In addition, the peaks placed at approximately 1450, 1535, and 1620 cm^{-1} can be identified as the aromatic C-N vibration [36,44,45]. The peak appearing at 810 cm^{-1} has been associated with the out-plane vibration of the heptazine rings [43]. The sulfur-based COF led to a very different FTIR pattern. The wide band defined in the CN due to terminal $-NH_x$ and adsorbed water molecules was not registered in the COF, suggesting a complete condensation of the naphthalene diamino groups during the COF synthesis. The presence of the triazine group in the COF led to some vibrational peaks such as C = N at 1570 and 1504 cm^{-1}, C-N stretch at 1357 cm^{-1}, C-H bend at 780 cm^{-1}, and C-O-C stretch leading to peaks at 1294 and 1155 cm^{-1}. The peak placed at 625 cm^{-1} may be attributed to C-S-C vibration.

To further investigate the structural properties of the samples, Raman spectroscopy was conducted, see spectra in Fig. 2**C**. The sample CN described the typical reported Raman spectrum of graphitic carbon nitride. The Raman peaks located at 707 cm^{-1} and 979 cm^{-1} are attributed to the breathing modes of the s-triazine ring which describe the out-of-plane deformation vibration between the layer of the g-C_3N_4 heterocycles [59]. The peak at 480 cm^{-1} is associated with the twisting vibration of the heptazine ring [60]. The peak at 1227 cm^{-1} can be ascribed to the double N = C (sp^2) bending vibration.[60] However, those samples modified with the insertion of the COF led to the absence of Raman peaks, as shown for 20 %COF-CN.

The textural properties were assessed by N_2 adsorption–desorption isotherms conducted at −196 °C. The physisorption isotherms are depicted in Fig. 3 and the textural properties are summarized in Table 1. A typical type IV pattern behavior with an H3 hysteresis loop [61–63] is described by the CN sample, as compatible with a mesoporous solid

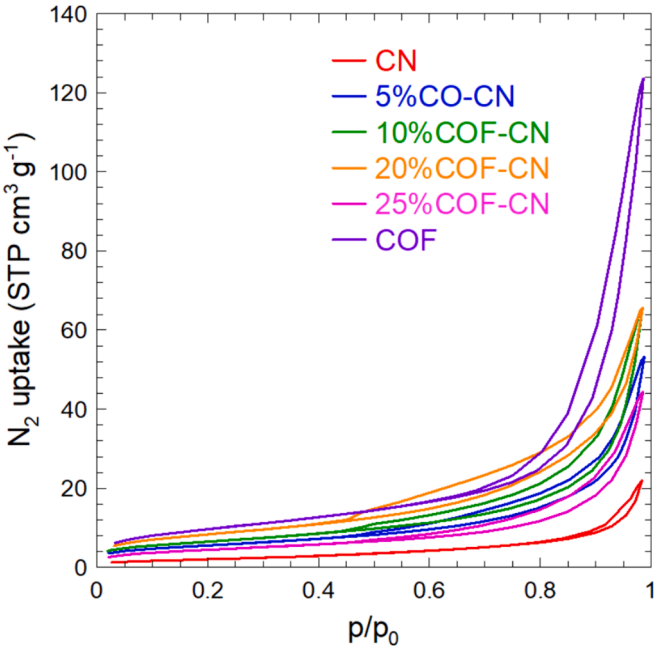

Fig. 3. N_2 adsorption–desorption isotherms of the COF-CN heterostructures.

composed of plate-like aggregates [64]. The BET area was as low as 7.7 m^2/g and poor pore volume, 0.034 $cm^3\ g^{-1}$, was found, typical values reported for graphitic carbon nitride prepared from the polymerization of melamine [65]. The COF displayed a higher specific area, 35.2 m^2/g, and an increased pore volume, i.e. 0.191 $cm^3\ g^{-1}$, defined its totality as mesopore. The COF-CN heterostructures performed textural values in between the obtained by CN and COF.

The elemental composition of the samples is available in Table 1. The C:N (at.) ratio of CN was 1.5, slightly higher than the theoretically expected for graphitic-like carbon nitride, but very similar to the value reported in other works using melamine as the precursor [8]. This ratio was gradually reduced as the proportion of the COF was raised.

The surface chemical environment was analyzed by XPS. The samples CN, COF, and 20 %COF-CN were selected for a detailed analysis and their XPS spectra after deconvolution are depicted in Fig. 4. The C_{1s} region of graphitic-like carbon nitride is commonly deconvoluted in three main contributions, i.e. a peak of sp^2 bonds linked to N-C=N bonds (288 eV), a peak of sp^3 carbon in C-C/C-N bonds (285.5–286.0 eV), and a peak of sp^2 carbon bonds present in aromatic C-C/C=C (~284.4 eV) [8,66]. According to the C_{1s} spectrum of CN, the contribution of N-C = N, representative of the triazine rings outstands from the rest, as reported in the literature for carbon nitrides prepared from melamine as a precursor [7,8]. In the case of the COF, the aromatic C-C/C=C bonds displayed more importance in the C_{1s} spectrum, due to the presence of the aromatic rings of naphthalene rings. The sp^3 contribution observed

Table 1
Crystal and textural properties, elemental composition, and optical properties of CN-COF heterostructures.

Sample	$L_{crystal}$ (nm)	d (Å)	n	S_{BET} ($m^2\ g^{-1}$)	V_T ($cm^3\ g^{-1}$)	C_{EA} (wt. %)	N_{EA} (wt. %)	S_{EA} (wt.)	N/C (at.)	E_{BG} (eV)
CN	12.93	3.248	40	7.7	0.034	34.2	59.7	0.0	1.50	2.55
5 %COF-CN	15.81	3.250	47	19.2	0.082	36.0	59.0	0.0	1.40	2.55
10 %COF-CN	11.86	3.245	37	23.4	0.101	38.5	56.4	0.2	1.26	2.50
20 %COF-CN	12.20	3.252	38	30.1	0.102	39.8	54.4	1.0	1.17	2.35
25 %COF-CN	14.73	3.238	45	16.4	0.069	37.1	54.5	1.9	1.26	2.35
COF	70.35	4.126	–	35.2	0.191	46.0	39.0	7.4	–	2.20

$L_{crystal}$, crystallite size from the highest peak by Scherrer's equation; d, interlayer spacing from the highest peak; n, number of layers; S_{BET}, specific total surface area obtained from the BET method; V_T, total pore volume obtained from the N_2 uptake at $p/p_0 \sim 0.99$; C, N, and S composition from elemental analysis (EA); and E_{BG}, bandgap energy estimated from the Tauc plot method.

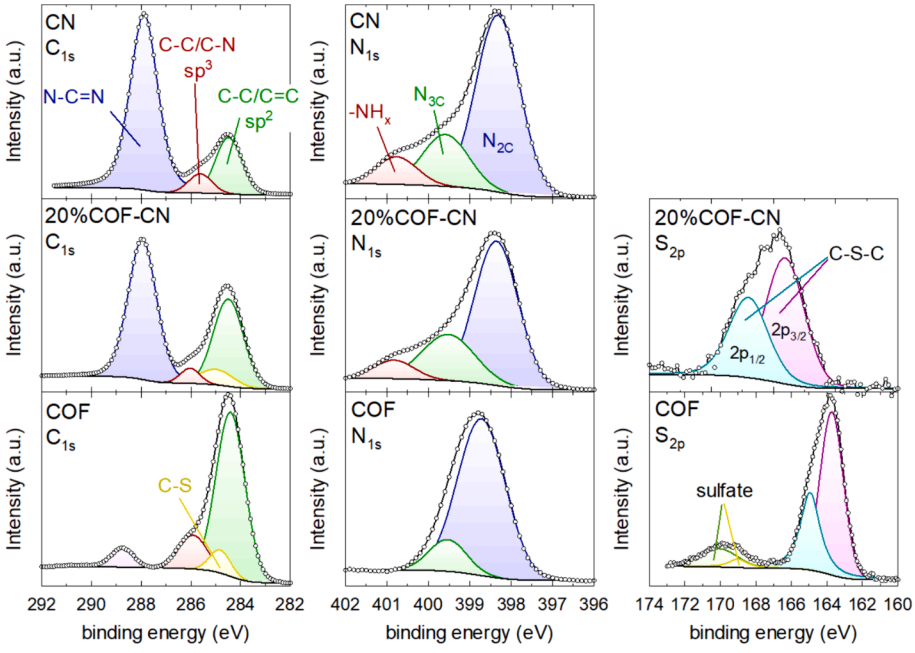

Fig. 4. High-resolution XPS spectra of C, N, and S regions for CN, COF, and 20 %COF-CN samples.

in the COF could be associated with the ether C-O-C bonds [67,68], much less intense than the aromatic sp^2 C-C contribution. A new peak due to the sulfur incorporation as C-S was added in the deconvolution of the C_{1s} region, placed at roughly 285.0 eV [26,69], leading to a peak with a similar area as the sp^3 C-O-C ether. Regarding the N_{1s} region, in the case of graphitic carbon nitride materials, three contributions can be ascribed, i.e. tertiary N from $(C)_3$–N rings (N_{3C}, 399.9 eV), sp^2-bonded in the form of N–C=N (N_{2C}, 398.4 eV), and terminal $-NH_x$ groups (400.8 eV) [54,70–73]. The predominant contribution observed in the CN sample was N_{2C} associated with the aromatic triazine rings, followed in importance by N_3C and terminal $-NH_x$, a behavior very similar to the already reported for this type of material [7,8]. The N_{1s} spectrum of the COF did not define amino $-NH_x$ groups and mostly N_2C, which could be attributed to the triazine units of the TFPC precursor of the COF. Finally, pertaining to the analysis of the S_{2p} region, a major contribution of thioether C-S-C was registered, with binding energies of 163.7 eV ($2_{p3/2}$) and 164.9 eV ($2_{p1/2}$) [69,74–77]. A minor contribution of sulfate was also registered, binding energies of 169.0 eV ($2_{p3/2}$) and 170.0 eV ($2_{p1/2}$) [78]. The heterostructure 20 %COF-CN displayed a contribution of both the CN and COF in the contributions of the above-mentioned regions, leading to a greater contribution of those provided by the CN due to the higher proportion if compared to the COF.

The morphology of some selected samples, i.e. CN, COF, and the 20 %COF-CN heterostructure, was studied by HR-STEM. The composition and distribution of the elements were also scanned by EDX mapping. Fig. 5 portrays some of the pictures obtained. The imaging of CN led to nanoparticles of different sizes up to 1 μm. In general, CN is characterized by the agglomeration of parallel sheets, in which a homogeneous distribution of C and N was appreciated. There was no obtained appreciable presence of oxygen in EDX analysis. The COF imaging depicted bigger aggregates of several micrometers. High-resolution imaging of these aggregates allowed us to define them as conglomerates of rod-shaped particles (see Fig. 5**E**). The heterostructure 20 %COF-CN led aggregates of similar size and shape as the COF. The EDX mapping draws a suitable picture of the heterogeneity of the sample. As the CN particles are richer in nitrogen than carbon, their presence in the heterostructure is enlightened by N-bright particles, attributable to laminar sheets of graphitic carbon nitride, as illustrated in the subfigures J-L of Fig. 5. The accumulation could be associated with the COF as the distribution of S suggests. Alternatively, the identification of the CN and COF areas in the heterostructure is demonstrated in the EDX spectrum, portrayed in subfigures M and N of Fig. 5, respectively. The presence of the COF helped to wrap CN particles in bigger aggregates, reaching an intimate contact between both components.

The optical properties were characterized by employing the DRS-UV–visible technique, leading to the absorption spectra depicted in Fig. 6**A**. As appreciated, the CN sample performed high absorbance in the UV region to dramatically decay at roughly 400 nm, describing an absorption peak around 300–400 nm. This peak can be attributed to the π–π * electronic transitions in the conjugated ring systems heptazine units [79], conferring to the material a yellowish aspect. The sulfur-based COF, of greenish aspect, displayed a strongly red-shifted spectrum beyond 800 nm. These results provide evidence of the boosted light-harvesting capability of the COF in a wide range of visible light region due to the delocalized π electrons in the polymeric structure, which is common in other triazine-based COFs [80]. The COF displayed two maximum absorption peaks, one placed at 300–400 nm similar to the CN sample and other broader at 500–800 nm, responsible of the greenish color of the material. The COF-CN heterojunctions displayed intermediate spectra, resembling the CN and COF depending on their relative proportion, being a raised amount of COF in the heterojunction positive for harvesting the radiation in the visible region. The bandgap values were determined by applying the Tauc plot method, see Fig. 6**B**. The COF displayed a lower band gap if compared to CN, 2.20 vs 2.35 eV. The 2.30 eV obtained for CN is lower than the typical 2.70 eV reported in the literature, probably due to the thermal treatment undergone in the microwave synthesis. The COF-CN heterostructures displayed intermediate bandgap values, as shown in Table 1, playing the COF with a decreasing effect.

3.2. *Photocatalytic activity of the COF-CN heterostructures*

The photocatalytic activity of the COF-CN heterostructures was tested for the degradation of acetaminophen. Fig. 7**A** depicts the results

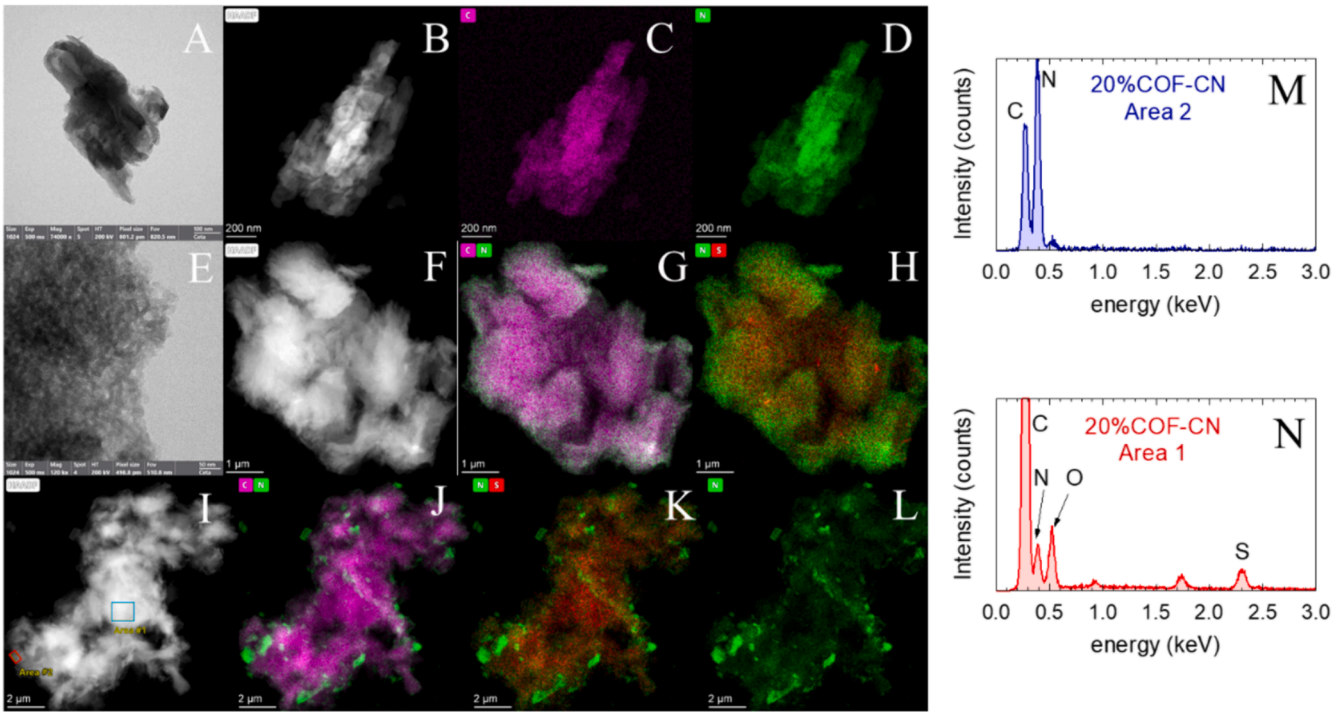

Fig. 5. HR-STEM images and EDX mapping of CN (A-D), COF (E-H), and 20 %COF-CN (I-L) and EDX spectra of selected areas of 20 %-COF-CN (M and N).

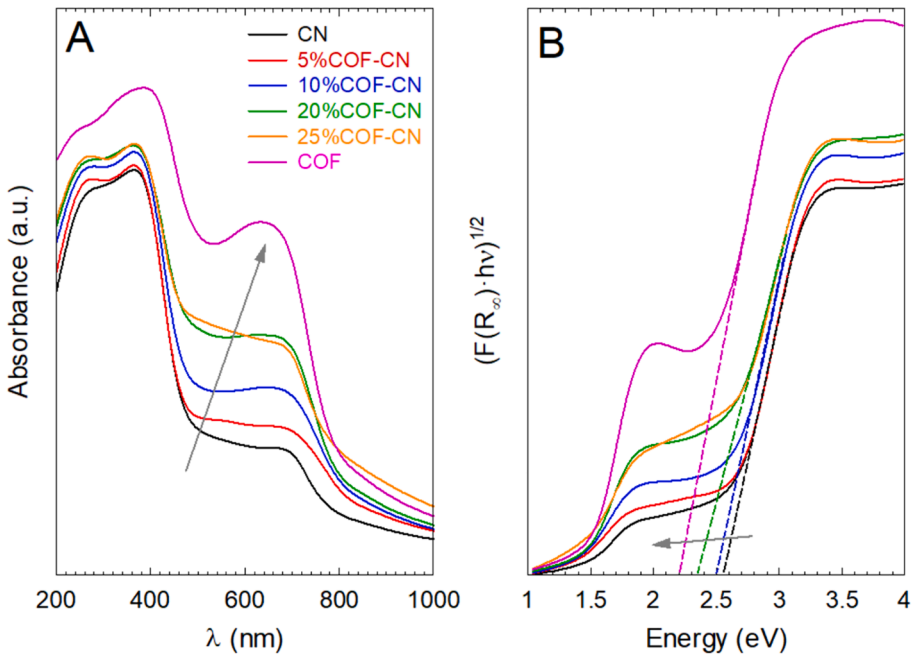

Fig. 6. DRS-UV–visible spectra (A) and determination of the band gap by the Tauc plot method (B) of the COF-CN heterostructures.

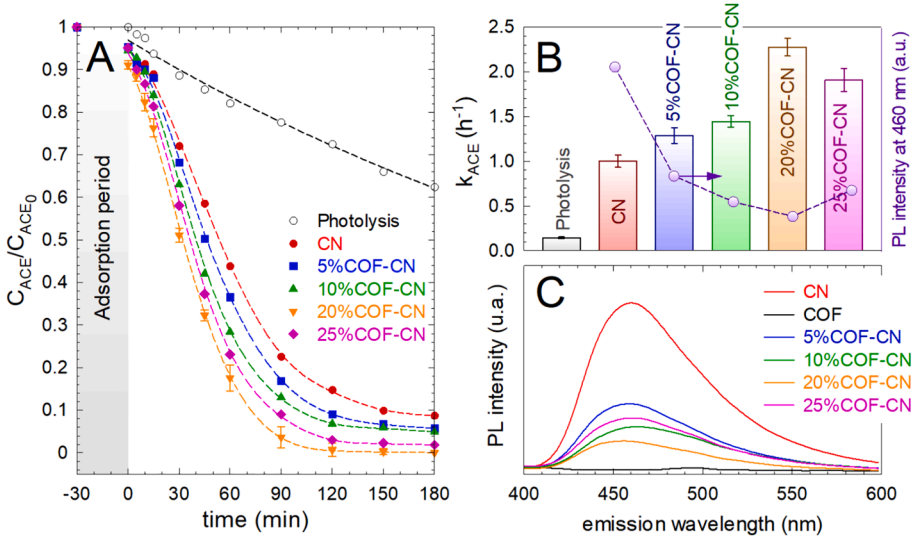

Fig. 7. Photocatalytic degradation of ACE with COF-CN heterostructures. Influence of the COF ratio on the temporal evolution of the normalized concentration (A), the pseudo-first order rate constant (B), and photoluminescence spectra (C). *Experimental conditions:* $V = 250$ *mL;* $T = 20$ °*C;* $C_{COF\text{-}CN} = 0.5$ *g/L;* $C_{ACE,0} = 5$ *mg/L.*

achieved. In the absence of radiation, ACE was slightly photolyzed, barely 38 %. The photocatalytic activity of carbon nitride led to roughly 90 % of the removal of ACE in 3 h, with a pseudo-first order rate constant of 1.00 h^{-1}, see Fig. 7**B**. Although the activity of the COF was tested, it led to insignificant degradation of ACE due to a lack of suspension of the COF in the aqueous sample. The high hydrophobicity of the COF forced the particles to be concentrated on the surface of the solution, discharging the possibility of its use without any modification in the structure. However, the incorporation of the COF in the CN structure enhanced the kinetics if compared to bare CN, due to the enhanced delocalization of the photogenerated charges, as proved in the reduction of the photoluminescence peak registered in the COF-CN heterostructures. The rise of COF ratio exerted a beneficial effect on the pseudo-first order rate constant, until reaching a maximum value of the $k = 2.28$ h^{-1} with the sample 20 %COF-CN, which supposes an overdoubled value concerning the CN sample. An excess of COF over 20 % worsened the results, as an excess of COF results in an excess of recombination of the electron-hole pair after excitation, as the photoluminescence spectra depicted in Fig. 7**C** of the sample 25 %COF-CN suggests. Furthermore, the evolution of the PL peak, whose maximum is defined at ca. 460 nm, can be correlated with the photocatalytic activity, leading to an inverse relationship between the pseudo-first order rate constant and the intensity of the PL peak, see Fig. 7**B**.

The kinetics performance obtained with the 20 %COF-CN sample was compared to the reported by similar materials in the literature, see Table 2. The tentative comparison should be taken with caution since the attained results considerably depend on the experimental conditions, i.e. nature of the radiation source and intensity. Notwithstanding the experimental conditions, the pseudo-first order rate constant $k_{ACE} = 2.28$ h^{-1} is within the same order of magnitude as other graphitic carbon nitride-based materials combined with TiO_2, or metal–organic frameworks. Other reported works have stated abnormally higher values that

Table 2
Comparison of the photocatalytic performance of acetaminophen degradation with similar materials.

Material	Radiation conditions	$C_{ACE,0}$ (mg/L)	$C_{catalyst}$ (g/L)	k_{ACE} (h^{-1})	Ref.
g-C_3N_4 based materials					
TiO_2/g-C_3N_4	UVA lamp (9 W) 365 nm	10.0	0.2	2.18	[81]
WO_3/g-C_3N_4	Xe lamp (300 W) >400 nm	10.0	1.0	7.80	[82]
CeO_2/I,K-g-C3N4	Visible (64 W) 465 nm	10.0	2.0	2.34	[83]
g-C_3N_4/UiO-66-NH_2	UVA lamps (18 W) 365 nm	5.0	0.5	2.00	[19]
g-C_3N_4/NH_2-MIL-101 (Fe)	Solar light (+H_2O_2)	20.0	0.4	6.90	[84]
Covalent Organic Frameworks materials					
COF based on phenylenediamine with 2 ortho heterocyclic N	Visible (125 W) >400 nm	5.0	0.3	7.68	[85]
Ketonenamine-based COF/ AgI	Xe lamp (300 W)	5.0	0.3	2.79	[86]
Sulfur-based thiazole-linked COF/ g-C_3N_4	UVA (18 W) 365 nm	5.0	0.5	2.28	This work
Metal Organic Frameworks materials					
UiO-66-NH_2	Xe lamp (600 W) > 320 nm	5.0	0.25	0.37	[87]
ZIF-8	Xe lamp (500 W) > 400 nm	1.0	0.5	0.14	[88]
NH_2-MIL-125(Ti-Zr)	Xe lamp (600 W) > 290 nm	5.0	0.25	0.73	[89]
Pd/NH_2-MIL-125	Xe lamp (600 W) > 290 nm	5.0	0.25	0.95	[90]
FeCo-MOF	Sunlight	20.0	0.5	1.86	[91]

can be attributed to more favorable radiation conditions, or the presence of highly active metallic species. The materials with the slowest kinetics were the metal–organic frameworks without combination with other semiconductors. Regarding covalent organic frameworks, there is scarce information about the photocatalytic degradation of contaminants of emerging concern; however, some of the reported k_{ACE} values are like those obtained with the synthesized material of this work.

The photoelectrochemical properties of the prepared COF-CN heterostructures were further characterized to reveal if the reason why the sample 20 %COF-CN outstands the rest is due to better electronic mobility, as tentatively suggested by the photoluminescence technique. The migration of charges, a crucial role during photocatalytic activation, was assessed by EIS characterization. Bearing in mind that the smaller radius curvature of the Nyquist plot means a higher mobility rate [48,92], as pictured in Fig. 8**A**, the addition of COF positively impacted a better electronic migration, resulting in lesser charge transfer resistance, which contributes to enhancing the charge migration. Concretely, the order of the radius depicted in the Nyquist diagram was 20 %COF-CN < 25 %COF-CN < 10 %COF-CN < 5 %COF-CN < CN. The lowest radius performed by 20 %COF-CN demonstrates the minimum resistance to electronic mobility and therefore the optimum ratio of COF added to the graphitic-like carbon nitride. Fig. 8**B** depicts the transient photocurrent response of the COF-CN samples for four on–off cycles under UVA radiation. It is well stated that the higher the photocurrent response, the higher the separation efficiency of the photo-generates charges [92]. The higher photocurrent intensity is also interpreted as a faster photo-excited electron transferred to the surface and less recombination of photoexcited electron-hole pair [93]. The order of photocurrent responses follows the results attained in the EIS analysis, since under illumination the photocurrent density was 20 %COF-CN > 25 %COF-CN > 10 %COF-CN > 5 %COF-CN > CN. It can be concluded, therefore, that the optimum COF ratio in the sample 20 %COF-CN displayed the lowest resistance to electronic mobility, the highest density of photogenerated charges under illumination, and the lowest recombination rate.

Fig. 9**A** illustrates the effect of the pH on the pseudo-first rate constant of ACE degradation (k_{ACE}) with 20 %COF-CN. As portrayed, the k_{ACE} values gradually augmented to reach the maximum value at circumneutral conditions and decreased at alkaline conditions. The ACE molecule displays a pKa = 9.5 [94], which means that the molecule is neutral in all the range of pH studied, therefore the electrostatic interactions do not pose relevant importance on the mechanism. At alkaline conditions, it has been stated a negative influence is due to the inhibition played by less effective migration of photogenerated charges at pH > 8 [95,96]. The 20 %COF-CN performs the best kinetics at close to neutral or slightly acidic conditions.

The presence of inorganic species such as Cl^-, NO_3^-, and HCO_3^- has been claimed to negatively interfere with the photocatalytic activity of

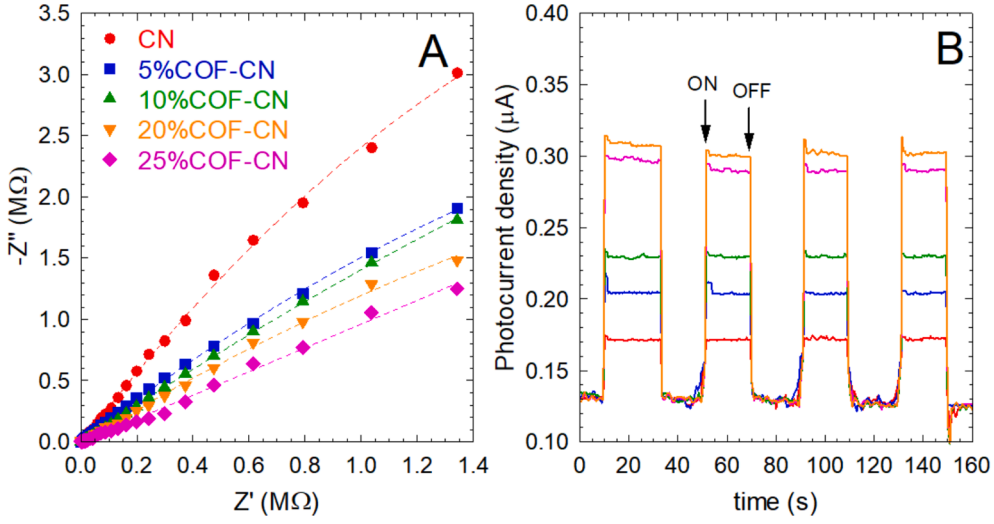

Fig. 8. Nyquist plot of electrochemical impedance spectroscopy (A) and transient photocurrent response (B) of COF-CN heterostructures.

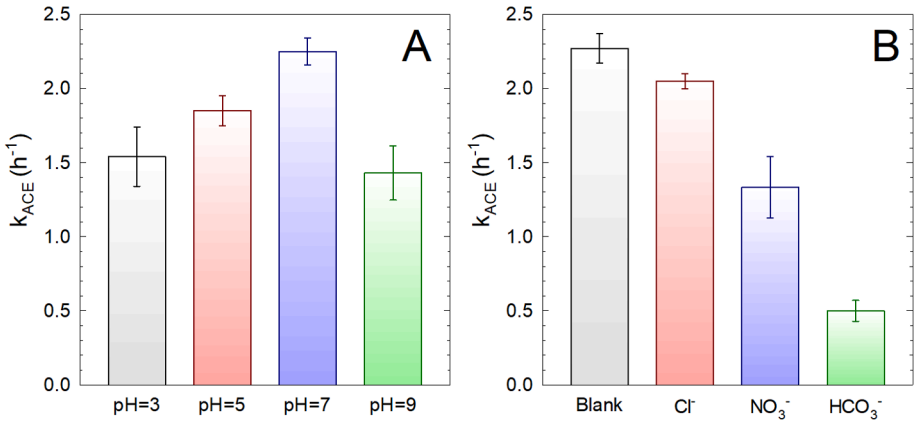

Fig. 9. Photocatalytic degradation of ACE with the 20 %COF-CN heterostructure. Influence of the pH (A) and the presence of anions (B) on the pseudo-first order rate constant. *Experimental conditions: V = 250 mL; T = 20 °C; $C_{20\%COF\text{-}CN}$ = 0.5 g/L; $C_{ACE,0}$ = 5 mg/L; pH = 3–9; C_{Cl^-}=2.5 mM; C_{NO3^-}=1 mM; C_{HCO3^-}=3 mM.*

photocatalysts due to their interaction with the generated reactive oxygen species. Accordingly, individual ACE degradation assays were conducted with 20 %COF-CN in the presence of the above-mentioned anions at their environmentally relevant concentration. The addition of Cl^- 2.5 mM displayed an unimportant effect whereas the presence of NO_3^- 1 mM exhibited a slight deceleration of the kinetics of ACE degradation, see the pseudo-first order rate constant variation in Fig. 9**B**. The presence of these anions in a photocatalytic process can lead to the formation of the less reactive species $Cl^{\bullet}$ and $NO_3^{\bullet}$, with the consequent quenching effect on the target contaminant degradation [97]. In the test carried out in the presence of HCO_3^-, the greatest decrease of the pseudo-first order rate constant was registered due to the combined effect of the less favorable pH, since the presence of HCO_3^- raised the pH to 8.5–9.0 and the formation of $CO_3^{\bullet -}$ radicals, which have demonstrated to possess lower reactivity, which often is considered as one of the main disadvantages for advanced oxidation technologies in practice [98].

Based on the boosted activity of the heterostructure 20 %COF-CN, additional tests were carried out to assess the behavior in the degradation of other contaminants of emerging concern (CEC). Fig. 10 shows the results attained during the degradation of a mixture of six CECs, i.e. acetaminophen, caffeine, antipyrine, ciprofloxacin, sulfamethoxazole, and diclofenac. For comparison purposes, a photolysis and the performance of the CN sample were also accomplished. Fig. 10**A** depicts the temporal evolution of the CEC concentration during the performance of photocatalytic degradation with 20 %COF-CN. As illustrated, ACE, CIP, and DCF were the most reactive, leading to a complete abatement in 120 min. In the case of DCF, a considerable adsorption contribution was registered in the previous 30 min of darkness step. DCF has been reported to be adsorbed onto carbon nitride [99], reaching mesoporous formulas with a maximum DCF uptake of up to 122 mg g^{-1} [100]. The other three contaminants, e.g. CAF, SMX, and ANT, showed more resistance to degradation. The recalcitrance of CAF [101] and ANT [102] towards photocatalytic oxidation has been widely reported in the literature. Interestingly, it is observed in their temporal profiles a slag period that coincides with the degradation of the three previously mentioned. Once a considerable removal, i.e. roughly 90 min of the most reactive is reached, the slope of the most recalcitrant increases (SMX, CAF, and ANT), defining kinetics adjustable to a pseudo-first order. Fig. 10**B** illustrates the pseudo-first order rate constant of photolysis, and photocatalytic oxidation with CN and 20 %COF-CN. From these results, it is also evidenced the easiness of the degradation of CIP, since it is simply removed by the sole action of radiation. CIP displays an important absorption activity between 300–350 nm [103,104], which makes it greatly sensitive for being photolyzed at 365 nm [105]. Excepting CIP, the rest of the CECs presented quite limited removal by photolysis. The photocatalytic oxidation of CN enhanced led to the removal of the CECs with a reactivity order DCF > CIP > ACE ≫ SMX > CAF > ANT. The

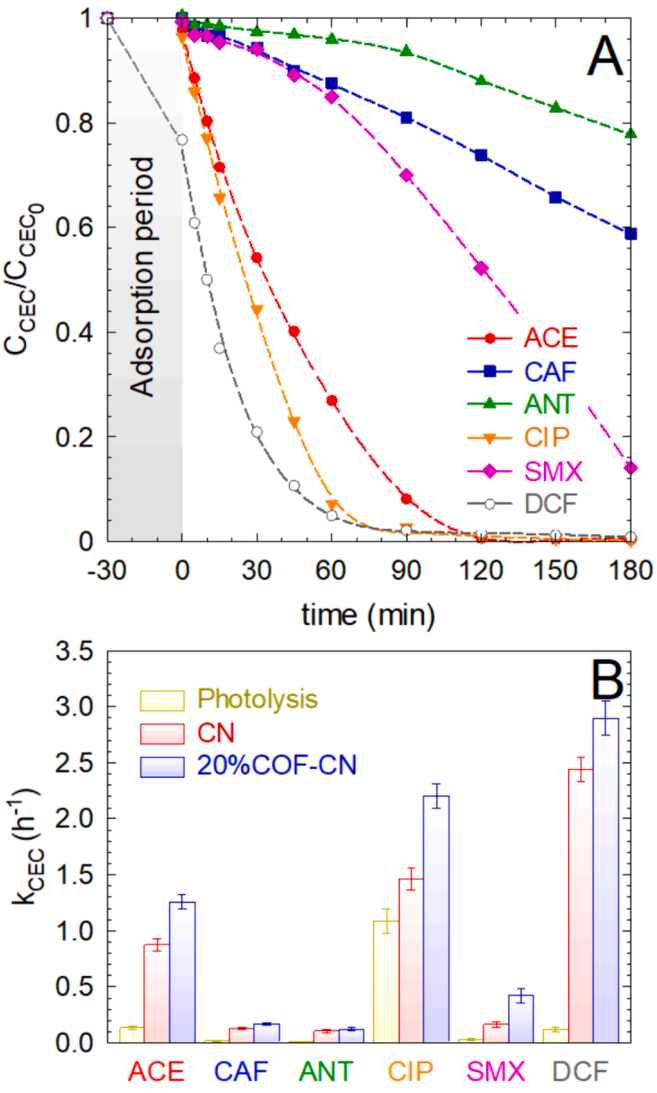

Fig. 10. Photocatalytic degradation of a mixture of six CECs with 20 %COF-CN heterostructure. Temporal evolution of the normalized concentration under photocatalytic degradation with 20 %COF-CN (A) and the pseudo-first order rate constant of photolysis, photocatalytic degradation with CN or 20 %COF-CN (B). *Experimental conditions: V = 250 mL; T = 20 °C; $C_{CATALYST}$ = 0.5 g/L (if necessary); $C_{CEC,0}$ = 2 mg/L (each).*

modification of the CN with the COF at the optimum ratio previously selected enhanced the kinetics of the photocatalytic degradation, raising for all the compounds the values of the k_{CEC} if compared to the bare CN.

The reusability of the 20 %COF-CN heterostructure was conducted by submitting the photocatalyst to sequential reuses of photocatalytic degradation of ACE. The temporal evolution of ACE concentration and the pseudo-first order rate constant linked to each cycle are depicted in Fig. 11A and B, respectively. After 5 reusing cycles, no appreciable loss of the activity in the removal of ACE was observed, leading to complete degradation of the contaminant after 180 min. Not only was the degradation degree stable, but most importantly, the kinetics did not show significant deterioration, i.e. the pseudo-first order rate constant values of ACE abatement were 2.3 ± 0.1 h^{-1} (run 0), 2.5 ± 0.2 h^{-1} (run 1), 2.3 ± 0.1 h^{-1} (run 2), 2.5 ± 0.2 h^{-1} (run 3), 2.4 ± 0.2 h^{-1} (run 4), and 2.3 ± 0.2 h^{-1} (run 5). The stability of the solid was additionally assessed in terms of the characterization of some of the structural properties. The XRD pattern of the sample recovered after the fifth run is depicted in Fig. 11**C**. As appreciated, there is no appreciable loss in the most characteristic peaks defined in the fresh 20 %COF-CN. The most intensive peak, e.g. the interlaying stacking plane (002), displayed almost the same intensity after the fifth use. Furthermore, the FTIR spectra were also recorded, see Fig. 11**D**. The footprint of both fresh and used after the fifth cycle was very similar, with practically the same definition of the vibration pattern. The optical properties (Fig. 11**E**) were almost unaltered, the bandgap being the same value after the fifth cycle of use.

3.3. Mechanism of photocatalytic activation of 20 %COF-CN heterostructure

The mechanism of photocatalytic performance of 20 %COF-CN was tentatively studied by evaluating the reactive oxidant species (ROS) involved in the process by adding chemical scavengers [106]. Fig. 12**A** illustrates the evolution of ACE with time for the blank test and in the presence of different scavengers, while Fig. 12**B** depicts the pseudo-first order rate constant in each test. The influence of the superoxide radical ($O_2^{\bullet -}$) was analyzed with three different strategies, i.e. by replacing the air bubbling with N_2, with the addition of p-benzoquinone (p-BZQ) or disodium 4,5-dihydroxybenzene-1,3-disulfonate (tiron). The release of $O_2^{\bullet -}$ is generated by the dissolved O_2 which is adsorbed in the surface of the photocatalyst and further reduced by the action of the photo-generated electrons. The dissolved O_2 was displaced by bubbling N_2, which led to a 74 % decrease in the k_{ACE} compared to the blank test. The addition of p-BZQ is extensively used in the scavengers' studies in photocatalytic processes [107], due to the high reactivity of this quinone with $O_2^{\bullet -}$, second-order rate constant $k_{p\text{-}BZQ,O2\bullet -}$=1 × 10^9 M^{-1} s^{-1} [108,109]. In the presence of p-BZQ the k_{ACE} was substantially declined, i.e. 92 %. The results obtained with p-BZQ should be taken with caution since they commonly lead to mistruths. p-BZQ can also react with $HO^{\bullet}$, even with faster kinetics, e.g. $k_{p\text{-}BZQ,HO\bullet}$=6.6 × 10^9 M^{-1} s^{-1} [110], and it suffers from photolysis under UVA radiation [111]. Furthermore, the photo-activation of p-BZQ has been reported to trigger the photo-reduction of quinones in water, yielding the formation of $HO^{\bullet}$ and semiquinone radicals, which hardens even more the interpretation of the results [112,113]. Consequently, an alternative scavenger such as tiron was used. Tiron has been labeled as a reliable alternative as it

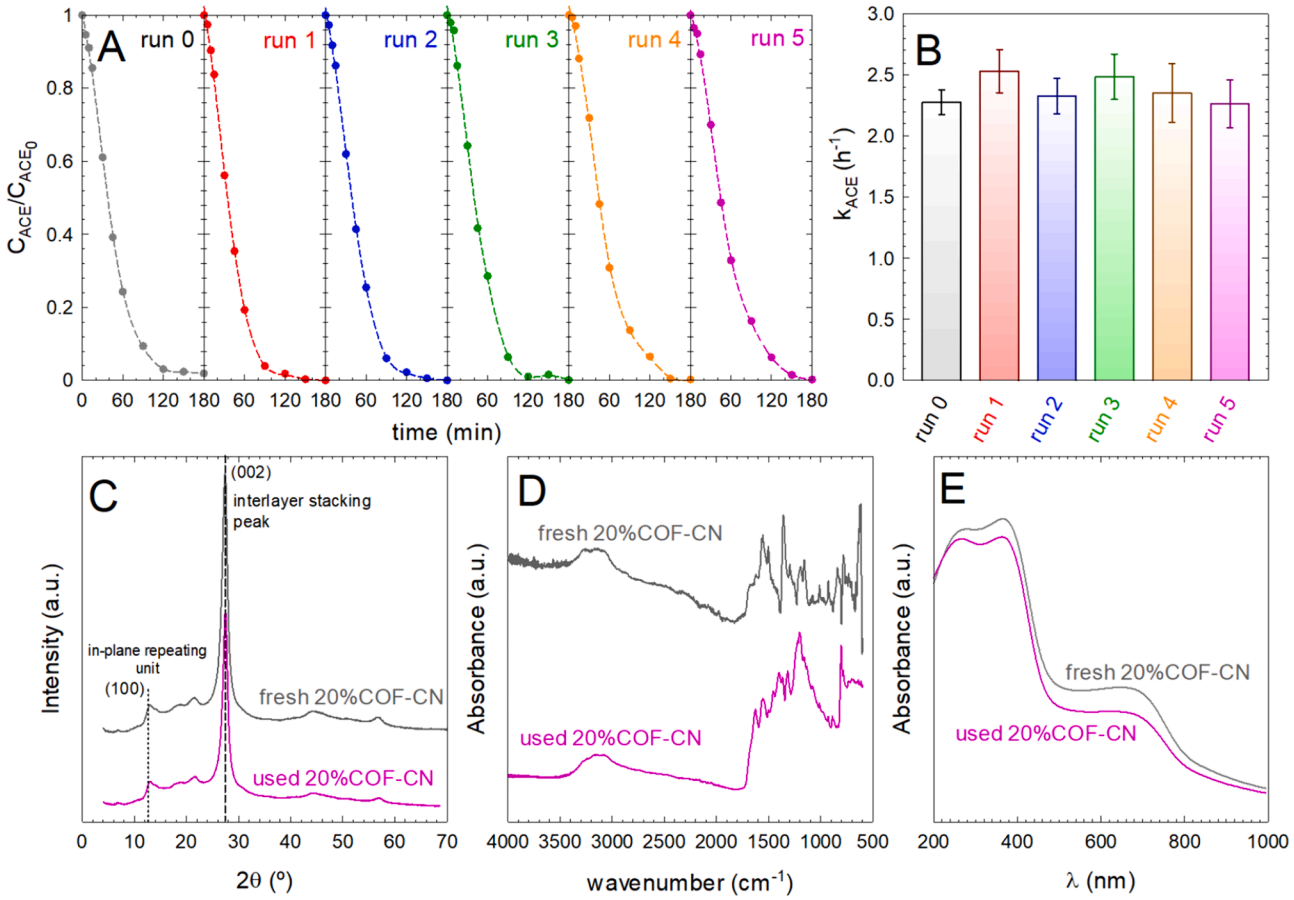

Fig. 11. Reusability and stability of 20 %COF-CN. Temporal evolution of ACE in sequential reuse cycles (A), the evolution of the pseudo-first order rate constant with the reuse cycles (B), changes in the XRD diffractograms (D), FTIR spectra (C), and DRS-UV–visible spectra (E) of fresh and the used 20 %COF-CN after the 5th run. *Experimental conditions of the reusing cycles: V = 250 mL; T = 20 °C; $C_{20\%COF\text{-}CN}$ = 0.5 g/L; $C_{ACE,0}$ = 5 mg/L.*

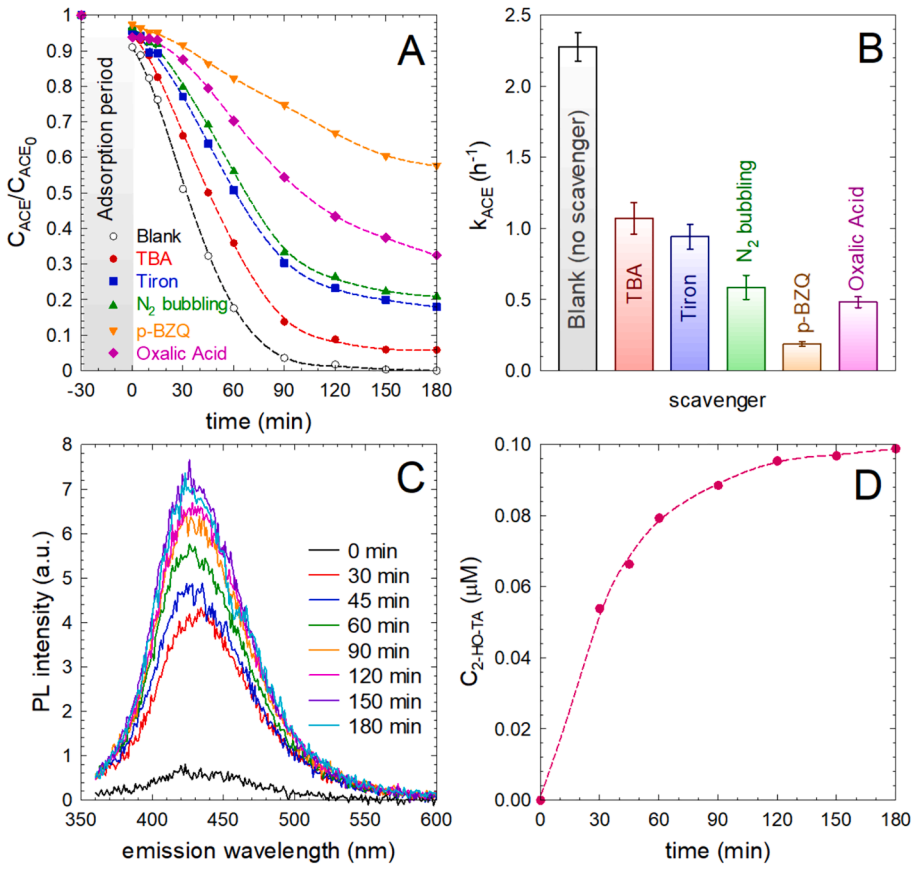

Fig. 12. Photocatalytic activity performance of 20 %COF-CN in the presence of chemical scavengers. Temporal evolution of ACE (A), and pseudo-first order rate constant (B) in the presence of scavengers. PL spectra of 2-HO-TPA (C) and temporal evolution of 2-HO-TA concentration (D). *Experimental conditions: V = 250 mL; T = 20 °C; $C_{20\%COF\text{-}CN}$ = 0.5 g/L; $C_{ACE,0}$ = 5 mg/L; $C_{scavenger}$ = 10 mM (TBA or oxalic acid) or 1 mM (tiron or p-BZQ), C_{TPA} = 1 mM.*

displays higher reactivity with superoxide radical if compared to hydroxyl radical, i.e. second-order rate constants $k_{tiron,O2\bullet-}$=5 × 10^9 M^{-1} s^{-1} [114], and $k_{tiron,HO\bullet}$=1.0 × 10^9 M^{-1} s^{-1} [115]. In the presence of tiron, the ACE photocatalytic degradation kinetic reduced the k_{ACE} to 58 %. Considering all the above, the role of $O_2^{\bullet-}$ could be observed as important, but not exclusive. The influence of HO• was assessed by the addition of *tert*-butyl alcohol (TBA), an alcohol able to trap HO• due to its high reactivity, e.g. second-order rate constant $k_{TBA,HO\bullet}$=6.2 × 10^8 M^{-1} s^{-1} [116]. In the presence of TBA, the k_{ACE} was reduced a 53 % compared to the blank test. According to this result, HO• also participates in the degradation process. To further confirm the presence of HO•, a probe method was conducted, monitoring the formation of the highly fluorescent 2-hydroxy-terephthalic acid (2-OH-TPA) from the selective reaction of HO• and terephthalic acid (TPA) [48,117–119]. According to the results portrayed in Fig. 12C-D, the production of hydroxyl radicals is quite limited. The maximum concentration of 2-HO-TPA reached was roughly 0.1 μM at 180 min, which is even lower than the estimated limit of detection for the photoluminescence method (0.21 μM). This concentration is one or two orders of magnitude lower than other systems in which the role played by hydroxyl radical is important [48,117,120]. However, these results disagree with the scavenger test carried out with TBA. Nonetheless, it should be considered that the results obtained from TBA may be misleading as the use of TBA overrates the importance of HO• [121] due to plausible adsorption of TBA onto the surface, competing with the target compound [112,122] or the release of organic radicals [121] that may overestimate the real impact of HO• in the medium. These considerations shed light on the little 2-HO-TPA observed in the probe test. Finally, the contribution of the photogenerated holes was evaluated by adding oxalate as hole-trapping agent [123]. The oxalate anion is adsorbed onto the surface of the photocatalyst, reacting with the holes and triggering the formation of CO_2 [41]. Although oxalate anions can also react with HO•, the kinetics is quite slow $k_{Oxalate,HO\bullet}$=1.5 × 10^7 M^{-1} s^{-1} [124], and the 2-HO-TPA probe method suggested a very limited impact of HO•. The performance of 20 %COF-CN under the addition of oxalic acid led to a decline of the k_{ACE} of about 79 %. In summary, the importance of the ROS involved in the process of ACE degradation with 20 %COF-CN was mainly holes and superoxide radicals, discharging the role played by hydroxyl radicals as the probe test pictured.

The band alignment of CN and the COF is proposed in Fig. 13. The Mott–Schottky plot, i.e. a graph of $1/C^2$ (C, the space charge capacitance) versus the potential, was carried out to estimate the flat band potential (V_{FB}) of both samples, as depicted in Fig. 13**A**. According to the Mott-Schottky equation simplified for semiconductors, it is possible to obtain V_{FB} from the intercept with the abscise axis (V_0) [125]. Usually, the V_{FB} is associated with the conduction band (V_{CB}) since the energy difference between both is much lower than the bandgap, being assumable the approximation with semiconductors of large bandgap [126]. Therefore, the conduction band can be estimated as follows:

$$V_{FB(NHE,\ pH)} \approx V_{CB(NHE,\ pH)} = V_0 - \frac{kT}{e} \quad (1)$$

where $V_{FB\ (NHE,\ pH)}$ means the flat band potential at the pH medium, V_0 is the potential at $1/C^2 = 0$, k stands for the Boltzmann's Constant, and T the temperature. The obtained V_{FB} was referenced to the normal hydrogen electrode (NHE) by adding the redox potential of Ag/AgCl ($\Delta V_{Ag/AgCl}$ = 0.21 V):

$$V_{CB(NHE,\ pH=7)} = V_{CB(NHE,\ pH)} + \Delta V_{Ag/AgCl} \quad (2)$$

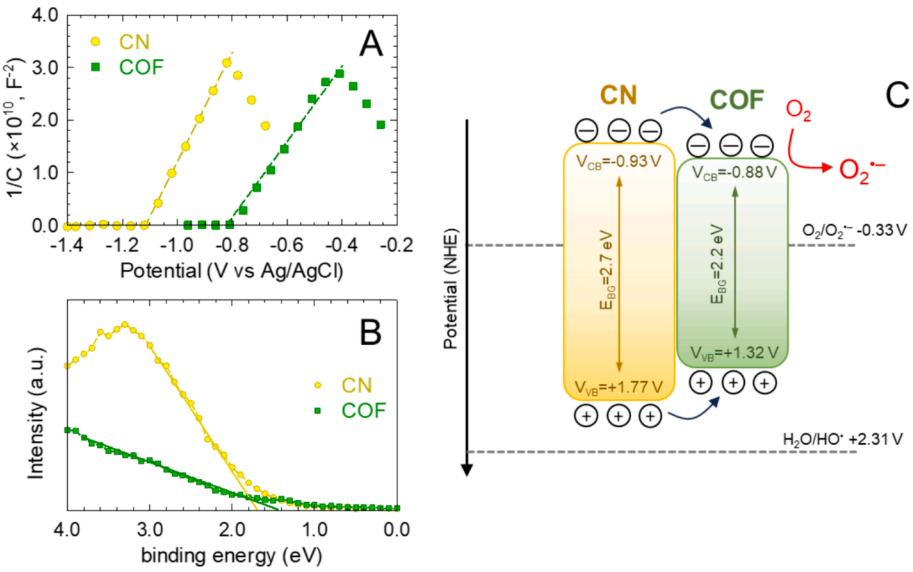

Fig. 13. Motty-Schottky plot for the determination of the flat band potential (A), estimation of the valence band edge by XPS (B), and proposal of bands alignment of CN and COF heterojunction (C).

The values obtained for the conduction band referred to as NHE were −0.93 V and −0.88 V for bare CN and COF, respectively. The potential of the valence band (V_{VB}) was determined by the addition of the energy of the bandgap obtained by DRS-UV–vis and the Tauc plot method [127]:

$$V_{VB} = V_{CB} + E_{BG} \quad (3)$$

Alternatively, the valence band edge has been estimated by the XPS analysis, recording at low binding energy values. Fig. 13**C** depicts the proposal of bandgap alignment according to the values obtained by electrochemical measurement for the V_{CB} and the bandgap values. Since the values of V_{CB} are close between CN and COF, and the bandgap is lower in the case of COF, a type I heterojunction can be defined in which under UVA radiation both are photo-excited, but an exchange of photogenerated electrons and holes from the CN to the COF can take place [128]. As portrayed in the band alignment, the V_{CB} either of CN or the COF is more negative than the redox potential of the pair $O_2/O_2^{\bullet-}$, e.g. −0.33 V vs NHE at pH = 7 [129]. Bearing in mind the scavenging effect in the presence of p-BZQ, tiron of N_2 bubbling, superoxide radicals are expected to be generated in the conduction band. The estimated values for the V_{VB} by electrochemical measurements were + 1.77 and + 1.32 V for CN and the COF, respectively. Alternatively, the energy of the valence band was also determined by XPS as the leading edge close to 0 eV binding energy of the photoemission spectra, as portrayed in Fig. 13 **B**. The values obtained were approximately + 1.65 and + 1.40 eV in CN and COF samples respectively. These values for the placement of the valence band prevent the formation of hydroxyl radicals, as reported in other materials [130]. The formation of hydroxyl radical is not expected since the location of the valence band would lead to the formation of holes whose potential is lower than the value required for the water molecule oxidation, i.e. the redox potential of the pair $H_2O/HO^{\bullet}$ is + 2.31 V vs NHE at pH = 7 [131]. This fact matches the low proportion of 2-HO-TPA monitored by photoluminescence which probes the negligible presence of hydroxyl radical in the aqueous medium. According to the scavengers' tests, the holes also play a relevant role by oxidizing the contaminant.

4. Conclusions

The sulfur-based thiazole-linked organic polymer prepared from the polycondensation of tri(4-formylphenoxy) cyanurate (TFPC) with sulfur and naphthalene diamine has been used satisfactorily for the preparation of a heterostructure in combination with graphitic-like carbon nitride under microwave-assisted synthesis. The resulting heterojunctions displayed enhanced photocatalytic activity towards the photocatalytic degradation of contaminants of emerging concern in water, overcoming the limitations of graphitic-like carbon nitride and the hydrophobicity of the COF. The COF-CN heterostructures performed larger activity in the degradation of acetaminophen than the non-modified CN, describing the sample 20 %COF-CN, i.e. 20 % (wt.) of COF in the material, an optimum COF:CN ratio. The 20 %COF-CN displayed the greatest degradation efficiency at nearly circumneutral conditions with only appreciable influence of HCO_3^- in the kinetics. This optimum sample verified the enhanced performance compared to the bare CN with diverse contaminants of emerging concern such as caffeine, antipyrine, ciprofloxacin, sulfamethoxazole, and diclofenac. The prepared heterojunctions displayed red-shifted UV–visible absorption spectra and lower photoluminescence response, which suggest a minimized effect of the undesirable recombination effect of the photogenerated charges. This behavior was further confirmed by electronic impedance spectroscopy, showing the heterojunction less resistance to the migration of charges; and was also corroborated by the higher transient photocurrent response under illumination. In these optical and electronic characterization analyses the sample 20 %COF-CN displayed the most beneficial performance among the rest, shedding light on the results achieved during the photocatalytic degradation tests.

The 20 %COF-CN sample demonstrated no appreciable loss of photocatalytic effectiveness in sequential recycling tests, in which the final recovered solid conserved the crystalline character and FTIR main vibration footprint of the fresh sample. The mechanism of photocatalytic oxidation was studied by the addition of chemical scavengers, depicting the key participation played by the superoxide radical and the photogenerated holes. The performance of hydroxyl radicals was discharged by a probe test analysis with terephthalic acid, dismissing the formation of 2-hydroxy-terephthalic acid. The determination of the conduction band potential with electrochemical measurements and the bandgap estimation allowed us to propose a band alignment of the CN and the COF, as a type I heterojunction. The presence of the COF would act as a sink of electrons, promoting the separation of charges. Either the conduction band of the CN and COF displayed a more negative potential than the pair $O_2/O_2^{\bullet-}$, supporting the relevance of superoxide radical in the mechanism. Furthermore, the lack of overlapping of $H_2O/HO^{\bullet}$ to the valence bands of the semiconductors, nor CN nor COF, corroborated the

lack of participation of hydroxyl radical, which matched with the probe test analysis with terephthalic acid.

The synthesis of free-metal photocatalysts through microwave-assisted methods overcomes the limitations of traditional solvothermal methods that rely on longer synthesis steps. The good activity and high stability make these novel materials competitive for further consideration in large-scale applications. However, extra attention regarding the design of effective photoreactors and the separation of the material are encouraged as prospects.

CRediT authorship contribution statement

Raziyeh Zandipak: Methodology, Investigation, Formal analysis, Conceptualization. **Nader Bahramifar:** Writing – review & editing, Validation, Supervision. **Morteza Torabi:** Writing – review & editing, Validation. **Mónica Calero:** Writing – review & editing, Supervision, Resources. **Mario J. Muñoz-Batista:** Writing – review & editing, Validation, Supervision, Methodology, Funding acquisition. **Rafael R. Solís:** Conceptualization, Investigation, Methodology, Formal analysis, Supervision, Writing – original draft, Funding acquisition.

Declaration of competing interest

The authors declare that they have no known competing financial interests or personal relationships that could have appeared to influence the work reported in this paper.

Data availability

Data will be made available on request.

Acknowledgments

The authors are grateful to the University of Granada for the “Pre-competitive Research Projects for Young Researchers Modality A—Young Doctors” of the 2019 and 2021 calls of the UGR Researching Plan (PPJIA2019-09 and PPJIA2021-34 grants). Funding for open access charge: Universidad de Granada/CBUA.

References

[1] X. Yang, D. Wang, Photocatalysis: from fundamental principles to materials and applications, ACS Appl Energy Mater 1 (2018) 6657–6693, https://doi.org/10.1021/ACSAEM.8B01345.
[2] S.K. Loeb, P.J.J. Álvarez, J.A. Brame, E.L. Cates, W. Choi, J. Crittenden, D. D. Dionysiou, Q. Li, G. Li-Puma, X. Quan, D.L. Sedlak, T. David Waite, P. Westerhoff, J.H. Kim, The technology horizon for photocatalytic water treatment: sunrise or sunset? Environ Sci Technol 53 (2019) 2937–2947, https://doi.org/10.1021/acs.est.8b05041.
[3] K. Maeda, K. Domen, Photocatalytic water splitting: recent progress and future challenges, J. Phys. Chem. Lett. 1 (2010) 2655–2661, https://doi.org/10.1021/JZ1007966.
[4] R. Li, W. Zhang, K. Zhou, Metal–organic-framework-based catalysts for photoreduction of CO2, Adv. Mater. 30 (2018) 1–31, https://doi.org/10.1002/adma.201705512.
[5] R. Li, Photocatalytic nitrogen fixation: An attractive approach for artificial photocatalysis, Chin. J. Catal. 39 (2018) 1180–1188, https://doi.org/10.1016/S1872-2067(18)63104-3.
[6] D.L.T. Nguyen, M.A. Tekalgne, T.H.C. Nguyen, M.T.N. Dinh, S.S. Sana, A. N. Grace, M. Shokouhimehr, D.V.N. Vo, C.K. Cheng, C.C. Nguyen, S.Y. Kim, Q. Van Le, Recent development of high-performance photocatalysts for N2 fixation: A review, J Environ Chem Eng 9 (2021) 104997, https://doi.org/10.1016/J.JECE.2020.104997.
[7] R.R. Solís, M.A. Quintana, G. Blázquez, M. Calero, M.J. Muñoz-Batista, Ruthenium deposited onto graphitic carbon modified with boron for the intensified photocatalytic production of benzaldehyde, Catal Today 423 (2023) 114266, https://doi.org/10.1016/J.CATTOD.2023.114266.
[8] M.A. Quintana, R.R. Solís, M. Ángeles Martín-Lara, G. Blázquez, F. Mónica Calero, M.J. Muñoz-Batista, Enhanced boron modified graphitic carbon nitride for the selective photocatalytic production of benzaldehyde, Sep Purif Technol 298 (2022) 121613, https://doi.org/10.1016/J.SEPPUR.2022.121613.
[9] Z. Ding, X. Chen, M. Antonietti, X. Wang, Synthesis of transition metal-modified carbon nitride polymers for selective hydrocarbon oxidation, ChemSusChem 4 (2011) 274–281, https://doi.org/10.1002/CSSC.201000149.
[10] G. Palmisano, E. García-López, G. Marcì, V. Loddo, S. Yurdakal, V. Augugliaro, L. Palmisano, Advances in selective conversions by heterogeneous photocatalysis, Chem. Commun. 46 (2010) 7074–7089, https://doi.org/10.1039/C0CC02087G.
[11] A. Akhundi, A. Badiei, G.M. Ziarani, A. Habibi-Yangjeh, M.J. Muñoz-Batista, R. Luque, Graphitic carbon nitride-based photocatalysts: toward efficient organic transformation for value-added chemicals production, Mol. Catal. 488 (2020) 110902, https://doi.org/10.1016/J.MCAT.2020.110902.
[12] X. She, J. Wu, J. Zhong, H. Xu, Y. Yang, R. Vajtai, J. Lou, Y. Liu, D. Du, H. Li, P. M. Ajayan, Oxygenated monolayer carbon nitride for excellent photocatalytic hydrogen evolution and external quantum efficiency, Nano Energy 27 (2016) 138–146, https://doi.org/10.1016/J.NANOEN.2016.06.042.
[13] L. Jiang, X. Yuan, Y. Pan, J. Liang, G. Zeng, Z. Wu, H. Wang, Doping of graphitic carbon nitride for photocatalysis: A reveiw, Appl Catal B 217 (2017) 388–406, https://doi.org/10.1016/j.apcatb.2017.06.003.
[14] X. Feng, H. Chen, F. Jiang, X. Wang, Enhanced visible-light photocatalytic nitrogen fixation over semicrystalline graphitic carbon nitride: Oxygen and sulfur co-doping for crystal and electronic structure modulation, J Colloid Interface Sci 509 (2018) 298–306, https://doi.org/10.1016/J.JCIS.2017.09.026.
[15] D. Jang, S. Lee, N.H. Kwon, T. Kim, S. Park, K.Y. Jang, E. Yoon, S. Choi, J. Han, T. W. Lee, J. Kim, S.J. Hwang, S. Park, Preparation of carbon nitride nanotubes with P-doping and their photocatalytic properties for hydrogen evolution, Carbon N Y 208 (2023) 290–302, https://doi.org/10.1016/J.CARBON.2023.03.038.
[16] H. Starukh, P. Praus, Doping of graphitic carbon nitride with non-metal elements and its applications in photocatalysis, Catalysts 10 (2020) 1119, https://doi.org/10.3390/CATAL10101119.
[17] R. Kavitha, P.M. Nithya, S. Girish Kumar, Noble metal deposited graphitic carbon nitride based heterojunction photocatalysts, Appl Surf Sci 508 (2020) 145142, https://doi.org/10.1016/J.APSUSC.2019.145142.
[18] B. Chen, P. Li, S. Zhang, W. Zhang, X. Dong, F. Xi, J. Liu, The enhanced photocatalytic performance of Z-scheme two-dimensional/two-dimensional heterojunctions from graphitic carbon nitride nanosheets and titania nanosheets, J Colloid Interface Sci 478 (2016) 263–270, https://doi.org/10.1016/j.jcis.2016.05.053.
[19] R.R. Solís, M.A. Quintana, M.Á. Martín-Lara, A. Pérez, M. Calero, M.J. Muñoz-Batista, Boosted activity of g-C_3N_4/UiO-66-NH_2 heterostructures for the photocatalytic degradation of contaminants in water, Int J Mol Sci 23 (2022) 12871, https://doi.org/10.3390/IJMS232112871/S1.
[20] S.M. Ghoreishian, G.S.R. Raju, K.S. Ranjith, H. Lee, C.H. Kwak, B. Park, S. Zeinali Nikoo, Y.K. Han, Y.S. Huh, Construction of 2D/2D/2D rGO/p-C_3N_4/$Cu_3Mo_2O_9$ heterostructure as an efficient catalytic platform for cascade photo-degradation and photoelectrochemical activity, Appl Surf Sci 511 (2020) 145469, https://doi.org/10.1016/J.APSUSC.2020.145469.
[21] Y. Shi, A.F. Yang, C.S. Cao, B. Zhao, Applications of MOFs: Recent advances in photocatalytic hydrogen production from water, Coord Chem Rev 390 (2019) 50–75, https://doi.org/10.1016/j.ccr.2019.03.012.
[22] J. Bedia, V. Muelas-Ramos, M. Peñas-Garzón, A. Gómez-Avilés, J.J. Rodríguez, C. Belver, A review on the synthesis and characterization of metal organic frameworks for photocatalytic water purification, Catalysts 9 (2019) 52, https://doi.org/10.3390/catal9010052.
[23] Z. Liang, R. Shen, Y.H. Ng, Y. Fu, T. Ma, P. Zhang, Y. Li, X. Li, Covalent organic frameworks: Fundamentals, mechanisms, modification, and applications in photocatalysis, Chem Catalysis 2 (2022) 2157–2228, https://doi.org/10.1016/J.CHECAT.2022.06.006.
[24] Q. Yang, M. Luo, K. Liu, H. Cao, H. Yan, Covalent organic frameworks for photocatalytic applications, Appl Catal B 276 (2020) 119174, https://doi.org/10.1016/J.APCATB.2020.119174.
[25] H. Wang, H. Wang, Z. Wang, L. Tang, G. Zeng, P. Xu, M. Chen, T. Xiong, C. Zhou, X. Li, D. Huang, Y. Zhu, Z. Wang, J. Tang, Covalent organic framework photocatalysts: structures and applications, Chem Soc Rev 49 (2020) 4135–4165, https://doi.org/10.1039/D0CS00278J.
[26] D.G. Wang, N. Li, Y. Hu, S. Wan, M. Song, G. Yu, Y. Jin, W. Wei, K. Han, G. C. Kuang, W. Zhang, Highly fluoro-substituted covalent organic framework and its application in lithium-sulfur batteries, ACS Appl Mater Interfaces 10 (2018) 42233–42240, https://doi.org/10.1021/ACSAMI.8B14213.
[27] M. Liu, L. Guo, S. Jin, B. Tan, Covalent triazine frameworks: synthesis and applications, J Mater Chem A Mater 7 (2019) 5153–5172, https://doi.org/10.1039/C8TA12442F.
[28] Y. An, X. Lv, W. Jiang, L. Wang, Y. Shi, X. Hang, H. Pang, The stability of MOFs in aqueous solutions—research progress and prospects, Green Chemical Engineering (2023), https://doi.org/10.1016/J.GCE.2023.07.004.
[29] G. Mouchaham, F.S. Cui, F. Nouar, V. Pimenta, J.S. Chang, C. Serre, Metal-organic frameworks and water: ‘from old enemies to friends’? Trends Chem 2 (2020) 990–1003, https://doi.org/10.1016/J.TRECHM.2020.09.004.
[30] Y. Ma, Y. Wang, H. Li, X. Guan, B. Li, M. Xue, Y. Yan, V. Valtchev, S. Qiu, Q. Fang, Three-dimensional chemically stable covalent organic frameworks through hydrophobic engineering, Angew. Chem. Int. Ed. 59 (2020) 19633–19638, https://doi.org/10.1002/ANIE.202005277.
[31] H. Bhambri, S. Khullar, S.K.M. Sakshi, Nitrogen-rich covalent organic frameworks: a promising class of sensory materials, Mater Adv 3 (2022) 19–124, https://doi.org/10.1039/D1MA00506E.
[32] L. Liao, M. Li, Y. Yin, J. Chen, Q. Zhong, R. Du, S. Liu, Y. He, W. Fu, F. Zeng, Advances in the synthesis of covalent triazine frameworks, ACS Omega 8 (2023) 4527–4542, https://doi.org/10.1021/ACSOMEGA.2C06961.

[33] Z. Lei, L.J. Wayment, J.R. Cahn, H. Chen, S. Huang, X. Wang, Y. Jin, S. Sharma, W. Zhang, Cyanurate-linked covalent organic frameworks enabled by dynamic nucleophilic aromatic substitution, J Am Chem Soc 144 (2022) 17737–17742, https://doi.org/10.1021/JACS.2C00778.

[34] P. Das, S.K. Mandal, A dual-functionalized, luminescent and highly crystalline covalent organic framework: molecular decoding strategies for VOCs and ultrafast TNP sensing, J Mater Chem A Mater 6 (2018) 16246–16256, https://doi.org/10.1039/C8TA05070H.

[35] T. He, W. Zhen, Y. Chen, Y. Guo, Z. Li, N. Huang, Z. Li, R. Liu, Y. Liu, X. Lian, C. Xue, T.C. Sum, W. Chen, D. Jiang, Integrated interfacial design of covalent organic framework photocatalysts to promote hydrogen evolution from water, Nature Communications 1 (14) (2023) 1–11, https://doi.org/10.1038/s41467-023-35999-y.

[36] A. Akhundi, A. Habibi-Yangjeh, M. Abitorabi, S. Rahim Pouran, Review on photocatalytic conversion of carbon dioxide to value-added compounds and renewable fuels by graphitic carbon nitride-based photocatalysts, Catal. Rev. 61 (2019) 595–628, https://doi.org/10.1080/01614940.2019.1654224.

[37] X. Wang, S. Blechert, M. Antonietti, Polymeric graphitic carbon nitride for heterogeneous photocatalysis, ACS Catal 2 (2012) 1596–1606, https://doi.org/10.1021/CS300240X.

[38] R.R. Solís, A. Gómez-Avilés, C. Belver, J.J. Rodriguez, J. Bedia, Microwave-assisted synthesis of NH2-MIL-125(Ti) for the solar photocatalytic degradation of aqueous emerging pollutants in batch and continuous tests, J Environ Chem Eng 9 (2021) 106230, https://doi.org/10.1016/J.JECE.2021.106230.

[39] R.R. Solís, M. Peñas-Garzón, C. Belver, J.J. Rodriguez, J. Bedia, Highly stable UiO-66-NH_2 by the microwave-assisted synthesis for solar photocatalytic water treatment, J Environ Chem Eng 10 (2022) 107122, https://doi.org/10.1016/J.JECE.2021.107122.

[40] Á. Pérez-Molina, L.M. Pastrana-Martínez, S. Morales-Torres, F.J. Maldonado-Hódar, Photodegradation of cytostatic drugs by g-C_3N_4: Synthesis, properties and performance fitted by selecting the appropriate precursor, Catal Today 418 (2023) 114068, https://doi.org/10.1016/J.CATTOD.2023.114068.

[41] J. Liqiang, Q. Yichun, W. Baiqi, L. Shudan, J. Baojiang, Y. Libin, F. Wei, F. Honggang, S. Jiazhong, Review of photoluminescence performance of nano-sized semiconductor materials and its relationships with photocatalytic activity, Sol. Energy Mater. Sol. Cells 90 (2006) 1773–1787, https://doi.org/10.1016/J.SOLMAT.2005.11.007.

[42] M. Anpo, M. Che, Applications of photoluminescence techniques to the characterization of solid surfaces in relation to adsorption, catalysis, and photocatalysis, Adv. Catal. 44 (1999) 119–257, https://doi.org/10.1016/S0360-0564(08)60513-1.

[43] H.N. Phong Vo, G.K. Le, T.M. Hong Nguyen, X.T. Bui, K.H. Nguyen, E.R. Rene, T. D.H. Vo, N.D. Thanh Cao, R. Mohan, Acetaminophen micropollutant: Historical and current occurrences, toxicity, removal strategies and transformation pathways in different environments, Chemosphere 236 (2019) 124391, https://doi.org/10.1016/J.CHEMOSPHERE.2019.124391.

[44] R. Montes, S. Méndez, J. Cobas, N. Carro, T. Neuparth, N. Alves, M.M. Santos, J. B. Quintana, R. Rodil, Occurrence of persistent and mobile chemicals and other contaminants of emerging concern in Spanish and Portuguese wastewater treatment plants, transnational river basins and coastal water, Sci. Total Environ. 885 (2023) 163737, https://doi.org/10.1016/J.SCITOTENV.2023.163737.

[45] Y. Tang, Y. Zhong, H. Li, Y. Huang, X. Guo, F. Yang, Y. Wu, Contaminants of emerging concern in aquatic environment: Occurrence, monitoring, fate, and risk assessment, Water Environ. Res 92 (2020) 1811–1817, https://doi.org/10.1002/WER.1438.

[46] M. Peñas-Garzón, W.H.M. Abdelraheem, C. Belver, J.J. Rodriguez, J. Bedia, D. D. Dionysiou, TiO_2-carbon microspheres as photocatalysts for effective remediation of pharmaceuticals under simulated solar light, Sep Purif Technol 275 (2021) 119169, https://doi.org/10.1016/J.SEPPUR.2021.119169.

[47] K.I. Ishibashi, A. Fujishima, T. Watanabe, K. Hashimoto, Detection of active oxidative species in TiO_2 photocatalysis using the fluorescence technique, Electrochem Commun 2 (2000) 207–210, https://doi.org/10.1016/S1388-2481(00)00006-0.

[48] A. Gómez-Avilés, R.R. Solís, E.M. García-Frutos, J. Bedia, C. Belver, Novel isoreticular UiO-66-NH_2 frameworks by N-cycloalkyl functionalization of the 2-aminoterephtalate linker with enhanced solar photocatalytic degradation of acetaminophen, Chem. Eng. J. 461 (2023) 141889, https://doi.org/10.1016/J.CEJ.2023.141889.

[49] J.C. Barreto, G.S. Smith, N.H.P. Strobel, P.A. McQuillin, T.A. Miller, Terephthalic acid: A dosimeter for the detection of hydroxyl radicals in vitro, PL89–PL96, Life Sci 56 (1994), https://doi.org/10.1016/0024-3205(94)00925-2.

[50] M. Qamar, R.B. Elsayed, K.R. Alhooshani, M.I. Ahmed, D.W. Bahnemann, Chemoselective and highly efficient conversion of aromatic alcohols into aldehydes photo-catalyzed by Ag_3PO_4 in aqueous suspension under simulated sunlight, Catal Commun 58 (2015) 34–39, https://doi.org/10.1016/J.CATCOM.2014.08.025.

[51] F. Fina, S.K. Callear, G.M. Carins, J.T.S. Irvine, Structural investigation of graphitic carbon nitride via XRD and neutron diffraction, Chem. Mater. 27 (2015) 2612–2618, https://doi.org/10.1021/ACS.CHEMMATER.5B00411.

[52] X. Li, J. Zhang, L. Shen, Y. Ma, W. Lei, Q. Cui, G. Zou, Preparation and characterization of graphitic carbon nitride through pyrolysis of melamine, Appl Phys A Mater Sci Process 94 (2009) 387–392, https://doi.org/10.1007/S00339-008-4816-4.

[53] Y. Fei, N. Han, M. Zhang, F. Yang, X. Yu, L. Shi, A. Khataee, W. Zhang, D. Tao, M. Jiang, Facile preparation of visible light-sensitive layered g-C_3N_4 for photocatalytic removal of organic pollutants, Chemosphere 307 (2022) 135718, https://doi.org/10.1016/J.CHEMOSPHERE.2022.135718.

[54] E. Alwin, W. Nowicki, R. Wojcieszak, M. Zieliński, M. Pietrowski, Elucidating the structure of the graphitic carbon nitride nanomaterials via X-ray photoelectron spectroscopy and X-ray powder diffraction techniques, Dalton Trans. 49 (2020) 12805–12813, https://doi.org/10.1039/D0DT02325F.

[55] Y. Lan, Z. Li, D. Li, G. Yan, Z. Yang, S. Guo, Graphitic carbon nitride synthesized at different temperatures for enhanced visible-light photodegradation of 2-naphthol, Appl Surf Sci 467–468 (2019) 411–422, https://doi.org/10.1016/J.APSUSC.2018.10.152.

[56] S.M. Ghoreishian, K.S. Ranjith, M. Ghasemi, B. Park, S.K. Hwang, N. Irannejad, M. Norouzi, S.Y. Park, R. Behjatmanesh-Ardakani, S.M. Pourmortazavi, S. Mirsadeghi, Y.K. Han, Y.S. Huh, Engineering the photocatalytic performance of B-C_3N_4@Bi_2S_3 hybrid heterostructures for full-spectrum-driven Cr(VI) reduction and in-situ H_2O_2 generation: Experimental and DFT studies, Chem. Eng. J. 452 (2023) 139435, https://doi.org/10.1016/J.CEJ.2022.139435.

[57] S. Horikoshi, A. Osawa, S. Sakamoto, N. Serpone, Control of microwave-generated hot spots. Part V. Mechanisms of hot-spot generation and aggregation of catalyst in a microwave-assisted reaction in toluene catalyzed by Pd-loaded AC particulates, Appl Catal A Gen 460–461 (2013) 52–60, https://doi.org/10.1016/J.APCATA.2013.04.022.

[58] Y. Liu, L. Jiang, Y. Tian, Z. Xu, W. Wang, M. Qiu, H. Wang, X. Li, G. Zhu, Y. Wang, Covalent organic framework/g-C_3N_4 van der Waals heterojunction toward H_2 production, Inorg Chem 62 (2023) 3271–3277, https://doi.org/10.1021/ACS.INORGCHEM.2C04366.

[59] M.Z. Rahman, J. Ran, Y. Tang, M. Jaroniec, S.Z. Qiao, Surface activated carbon nitride nanosheets with optimized electro-optical properties for highly efficient photocatalytic hydrogen production, J Mater Chem A Mater 4 (2016) 2445–2452, https://doi.org/10.1039/C5TA10194H.

[60] J. Jiang, L. Ou-Yang, L. Zhu, A. Zheng, J. Zou, X. Yi, H. Tang, Dependence of electronic structure of g-C_3N_4 on the layer number of its nanosheets: A study by Raman spectroscopy coupled with first-principles calculations, Carbon N Y 80 (2014) 213–221, https://doi.org/10.1016/J.CARBON.2014.08.059.

[61] K.S.W. Sing, R.T. Williams, Physisorption hysteresis loops and the characterization of nanoporous materials, Adsorpt. Sci. Technol. 22 (2016) 773–782, https://doi.org/10.1260/0263617053499032.

[62] K.S.W. Sing, D.H. Everett, R.A.W. Haul, L. Moscou, R.A. Pierotti, J. Rouquerol, T. Siemieniewska, Reporting physisorption data for gas/solid systems with special reference to the determination of surface area and porosity, Pure Appl. Chem. 57 (1985) 603–619, https://doi.org/10.1351/PAC198557040603.

[63] M. Thommes, K. Kaneko, A.V. Neimark, J.P. Olivier, F. Rodríguez-Reinoso, J. Rouquerol, K.S.W.W. Sing, Physisorption of gases, with special reference to the evaluation of surface area and pore size distribution (IUPAC Technical Report), Pure Appl. Chem. 87 (2015) 1051–1069.

[64] P. Babu, S. Mohanty, B. Naik, K. Parida, Synergistic effects of boron and sulfur co-doping into graphitic carbon nitride framework for enhanced photocatalytic activity in visible light driven hydrogen generation, Applied Energy Materials 1 (2018) 5936–5947, https://doi.org/10.1021/acsaem.8b00956.

[65] H. Cai, D. Han, X. Wang, X. Cheng, J. Liu, L. Jia, Y. Ding, S. Liu, X. Fan, High specific surface area defective g-C_3N_4 nanosheets with enhanced photocatalytic activity prepared by using glyoxylic acid mediated melamine, Mater Chem Phys 256 (2020) 123755, https://doi.org/10.1016/J.MATCHEMPHYS.2020.123755.

[66] Y. Wen, D. Qu, L. An, X. Gao, W. Jiang, D. Wu, D. Yang, Z. Sun, Defective g-C_3N_4 prepared by the $NaBH_4$ reduction for high-performance H_2 production, ACS Sustain Chem Eng 7 (2019) 2343–2349, https://doi.org/10.1021/ACSSUSCHEMENG.8B05124.

[67] L.D. Ramírez-Valencia, E. Bailón-García, A.I. Moral-Rodríguez, F. Carrasco-Marín, A.F. Pérez-Cadenas, Carbon gels-green graphene composites as metal-free bifunctional electro-fenton catalysts, Gels 9 (2023) 665, https://doi.org/10.3390/GELS9080665.

[68] M. Smith, L. Scudiero, J. Espinal, J.S. McEwen, M. Garcia-Perez, Improving the deconvolution and interpretation of XPS spectra from chars by ab initio calculations, Carbon N Y 110 (2016) 155–171, https://doi.org/10.1016/J.CARBON.2016.09.012.

[69] C. Varodi, F. Pogăcean, A. Cioriță, O. Pană, C. Leoștean, B. Cozar, T. Radu, M. Coroș, R.I. Ștefan-Van Staden, S.M. Pruneanu, Nitrogen and sulfur co-doped graphene as efficient electrode material for L-cysteine detection, Chemosensors 9 (2021) 146, https://doi.org/10.3390/CHEMOSENSORS9060146.

[70] A.P. Dementjev, A. De Graaf, M.C.M. Van de Sanden, K.I. Maslakov, A. V. Naumkin, A.A. Serov, X-Ray photoelectron spectroscopy reference data for identification of the C_3N_4 phase in carbon–nitrogen films, Diam Relat Mater 9 (2000) 1904–1907, https://doi.org/10.1016/S0925-9635(00)00345-9.

[71] U. Caudillo-Flores, D. Rodríguez-Padrón, M.J. Muñoz-Batista, A. Kubacka, R. Luque, M. Fernández-García, Facile synthesis of B/g-C_3N_4 composite materials for the continuous-flow selective photo-production of acetone, Green Chem. 22 (2020) 4975–4984, https://doi.org/10.1039/D0GC01326A.

[72] H. Xu, Z. Wu, Y. Wang, C. Lin, Enhanced visible-light photocatalytic activity from graphene-like boron nitride anchored on graphitic carbon nitride sheets, J Mater Sci 52 (2017) 9477–9490, https://doi.org/10.1007/S10853-017-1167-6.

[73] Y. Duan, Y. Wang, L. Gan, J. Meng, Y. Feng, K. Wang, K. Zhou, C. Wang, X. Han, X. Zhou, Amorphous Carbon Nitride with Three Coordinate Nitrogen ($N3_C$) Vacancies for Exceptional NO_x Abatement in Visible Light, Adv Energy Mater 11 (2021) 2004001, https://doi.org/10.1002/AENM.202004001.

[74] M. Fantauzzi, B. Elsener, D. Atzei, A. Rigoldi, A. Rossi, Exploiting XPS for the identification of sulfides and polysulfides, RSC Adv 5 (2015) 75953–75963, https://doi.org/10.1039/C5RA14915K.

[75] X. Cao, X. Huang, J. Zeng, R. Zhang, H. Zhong, Z. Cao, Uncovering the roles of C-S-C group in improving the flotation performance of benzohydroxamic acid toward galena, Appl Surf Sci 608 (2023) 155197, https://doi.org/10.1016/J.APSUSC.2022.155197.

[76] S.Y. Ding, M. Dong, Y.W. Wang, Y.T. Chen, H.Z. Wang, C.Y. Su, W. Wang, Thioether-based fluorescent covalent organic framework for selective detection and facile removal of mercury(II), J Am Chem Soc 138 (2016) 3031–3037, https://doi.org/10.1021/JACS.5B10754.

[77] C.P. Adams, C.D.J. Bonner, G. Pathiraja, S.O. Obare, Room-temperature synthesis of thioether-stabilized ruthenium nanocubes and their optical properties, Langmuir 10 (2023) 11, https://doi.org/10.1021/ACS.LANGMUIR.2C02645.

[78] M. Wahlqvist, A. Shchukarev, XPS spectra and electronic structure of group IA sulfates, J Electron Spectros Relat Phenomena 156–158 (2007) 310–314, https://doi.org/10.1016/J.ELSPEC.2006.11.032.

[79] R. You, H. Dou, L. Chen, S. Zheng, Y. Zhang, Graphitic carbon nitride with S and O codoping for enhanced visible light photocatalytic performance, RSC Adv 7 (2017) 15842–15850, https://doi.org/10.1039/C7RA01036B.

[80] T. Liu, X. Hu, Y. Wang, L. Meng, Y. Zhou, J. Zhang, M. Chen, X. Zhang, Triazine-based covalent organic frameworks for photodynamic inactivation of bacteria as type-II photosensitizers, J Photochem Photobiol B 175 (2017) 156–162, https://doi.org/10.1016/J.JPHOTOBIOL.2017.07.013.

[81] E.D. Mohamed Isa, R. Rasit Ali, N.W. Che Jusoh, Y. Nagao, K. Aoki, S. Nishimura, Z.I. Ahmad Tarmizi, S.H. Mohd Taib, Enhanced paracetamol photodegradation over synthesized TiO2/g-C3N4 nanocomposites: Effect of g-C_3N_4 loading on the properties and performance, Colloids Surf A Physicochem Eng Asp 694 (2024) 134066, https://doi.org/10.1016/J.COLSURFA.2024.134066.

[82] J. Meng, X. Wang, Y. Liu, M. Ren, X. Zhang, X. Ding, Y. Guo, Y. Yang, Acid-induced molecule self-assembly synthesis of Z-scheme WO_3/g-C_3N_4 heterojunctions for robust photocatalysis against phenolic pollutants, Chem. Eng. J. 403 (2021) 126354, https://doi.org/10.1016/J.CEJ.2020.126354.

[83] L.K.B. Paragas, V. Dien Dang, R.S. Sahu, S. Garcia-Segura, M.D.G. de Luna, J.A. I. Pimentel, R.A. Doong, Enhanced visible-light-driven photocatalytic degradation of acetaminophen over CeO2/I, K-codoped C3N4 heterojunction with tunable properties in simulated water matrix, Sep Purif Technol 272 (2021) 117567, https://doi.org/10.1016/J.SEPPUR.2020.117567.

[84] D. Pattappan, K.V. Kavya, S. Vargheese, R.T.R. Kumar, Y. Haldorai, Graphitic carbon nitride/NH_2-MIL-101(Fe) composite for environmental remediation: Visible-light-assisted photocatalytic degradation of acetaminophen and reduction of hexavalent chromium, Chemosphere 286 (2022) 131875, https://doi.org/10.1016/J.CHEMOSPHERE.2021.131875.

[85] F. Liu, Z. Ma, Y. Deng, M. Wang, P. Zhou, W. Liu, S. Guo, M. Tong, D. Ma, Tunable covalent organic frameworks with different heterocyclic nitrogen locations for efficient Cr(VI) reduction, escherichia coli disinfection, and paracetamol degradation under visible-light irradiation, Environ Sci Technol 55 (2021) 5371–5381, https://doi.org/10.1021/ACS.EST.0C07857.

[86] F. Liu, C. Nie, Q. Dong, Z. Ma, W. Liu, M. Tong, AgI modified covalent organic frameworks for effective bacterial disinfection and organic pollutant degradation under visible light irradiation, J Hazard Mater 398 (2020) 122865, https://doi.org/10.1016/J.JHAZMAT.2020.122865.

[87] Y.L. Wang, S. Zhanb, Y.F. Zhab, J. Bedia, J.J. Rodriguez, C. Belver, UiO-66 based metal organic frameworks for the photodegradation of acetaminophen under simulated solar irradiation, J Environ Chem Eng 9 (2021) 106087, https://doi.org/10.1016/j.jece.2021.106087.

[88] G. Fan, X. Zheng, J. Luo, H. Peng, H. Lin, M. Bao, L. Hong, J. Zhou, Rapid synthesis of Ag/AgCl@ZIF-8 as a highly efficient photocatalyst for degradation of acetaminophen under visible light, Chem. Eng. J. 351 (2018) 782–790, https://doi.org/10.1016/J.CEJ.2018.06.119.

[89] A. Gómez-Avilés, M. Peñas-Garzón, J. Bedia, D.D. Dionysiou, J.J. Rodríguez, C. Belver, Mixed Ti-Zr metal-organic-frameworks for the photodegradation of acetaminophen under solar irradiation, Appl Catal B 253 (2019) 253–262, https://doi.org/10.1016/j.apcatb.2019.04.040.

[90] V. Muelas-Ramos, C. Belver, J.J. Rodriguez, J. Bedia, Synthesis of noble metal-decorated NH_2-MIL-125 titanium MOF for the photocatalytic degradation of acetaminophen under solar irradiation, Sep Purif Technol 272 (2021) 118896, https://doi.org/10.1016/J.SEPPUR.2021.118896.

[91] D. Pattappan, A. Mohankumar, R.T.R. Kumar, S. Palanisamy, Y.T. Lai, Y.S. Huh, J. J. Shim, Y. Haldorai, Visible light photocatalytic activity of a FeCo metal-organic framework for degradation of acetaminophen and 2,4-dichlorophenoxyacetic acid and a nematode-based ecological assessment, Chem. Eng. J. 464 (2023) 142676, https://doi.org/10.1016/J.CEJ.2023.142676.

[92] Q. Chen, R. Tong, X. Chen, Y. Xue, Z. Xie, Q. Kuang, L. Zheng, Ultrafine ZnO quantum dot-modified TiO_2 composite photocatalysts: the role of the quantum size effect in heterojunction-enhanced photocatalytic hydrogen evolution, Catal Sci Technol 8 (2018) 1296–1303, https://doi.org/10.1039/C7CY02310C.

[93] F. Wei, J. Li, C. Dong, Y. Bi, X. Han, Plasmonic Ag decorated graphitic carbon nitride sheets with enhanced visible-light response for photocatalytic water disinfection and organic pollutant removal, Chemosphere 242 (2020) 125201, https://doi.org/10.1016/J.CHEMOSPHERE.2019.125201.

[94] E. Dinç, Z.C. Ertekin, N. Ünal, Three-way analysis of pH-UV absorbance dataset for the determination of paracetamol and its pKa value in presence of excipients, Spectrochim Acta A Mol Biomol Spectrosc 230 (2020) 118049, https://doi.org/10.1016/J.SAA.2020.118049.

[95] Z.J. Li, Z.W. Huang, W.L. Guo, L. Wang, L.R. Zheng, Z.F. Chai, W.Q. Shi, Enhanced photocatalytic removal of uranium(VI) from aqueous solution by magnetic TiO_2/Fe_3O_4 and its graphene composite, Environ Sci Technol 51 (2017) 5666–5674, https://doi.org/10.1021/ACS.EST.6B05313.

[96] P. Mei, H. Wang, H. Guo, N. Zhang, S. Ji, Y. Ma, J. Xu, Y. Li, H. Alsulami, M. S. Alhodaly, T. Hayat, Y. Sun, The enhanced photodegradation of bisphenol A by TiO_2/C_3N_4 composites, Environ Res 182 (2020) 109090, https://doi.org/10.1016/J.ENVRES.2019.109090.

[97] Z. Hu, X. Cai, Z. Wang, S. Li, Z. Wang, X. Xie, Construction of carbon-doped supramolecule-based g-C_3N_4/TiO_2 composites for removal of diclofenac and carbamazepine: A comparative study of operating parameters, mechanisms, degradation pathways, J Hazard Mater 380 (2019) 120812, https://doi.org/10.1016/J.JHAZMAT.2019.120812.

[98] N. Liu, N. Lu, H.T. Yu, S. Chen, X. Quan, Enhanced degradation of organic water pollutants by photocatalytic in-situ activation of sulfate based on Z-scheme g-C_3N_4/$BiPO_4$, Chem. Eng. J. 428 (2022) 132116, https://doi.org/10.1016/J.CEJ.2021.132116.

[99] A.N. Oliveros, J.A.I. Pimentel, M.D.G. de Luna, S. Garcia-Segura, R.R.M. Abarca, R.A. Doong, Visible-light photocatalytic diclofenac removal by tunable vanadium pentoxide/boron-doped graphitic carbon nitride composite, Chem. Eng. J. 403 (2021) 126213, https://doi.org/10.1016/J.CEJ.2020.126213.

[100] T. Shojaeimehr, M. Tasbihi, A. Acharjya, A. Thomas, R. Schomäcker, M. Schwarze, Impact of operating conditions for the continuous-flow degradation of diclofenac with immobilized carbon nitride photocatalysts, J Photochem Photobiol A Chem 388 (2020) 112182, https://doi.org/10.1016/J.JPHOTOCHEM.2019.112182.

[101] L. Prieto-Rodriguez, S. Miralles-Cuevas, I. Oller, A. Agüera, G.L. Puma, S. Malato, Treatment of emerging contaminants in wastewater treatment plants (WWTP) effluents by solar photocatalysis using low TiO_2 concentrations, J Hazard Mater 211–212 (2012) 131–137, https://doi.org/10.1016/J.JHAZMAT.2011.09.008.

[102] O. Gimeno, J.F. García-Araya, F.J. Beltrán, F.J. Rivas, A. Espejo, Removal of emerging contaminants from a primary effluent of municipal wastewater by means of sequential biological degradation-solar photocatalytic oxidation processes, Chem. Eng. J. 290 (2016) 12–20, https://doi.org/10.1016/J.CEJ.2016.01.022.

[103] S.R. Batchu, V.R. Panditi, K.E. O'Shea, P.R. Gardinali, Photodegradation of antibiotics under simulated solar radiation: Implications for their environmental fate, Sci. Total Environ. 470–471 (2014) 299–310, https://doi.org/10.1016/j.scitotenv.2013.09.057.

[104] J. Zambrano, P.A. García-Encina, J.J. Jiménez, R. López-Serna, R. Irusta-Mata, Photolytic and photocatalytic removal of a mixture of four veterinary antibiotics, J. Water Process Eng. 48 (2022) 102841, https://doi.org/10.1016/J.JWPE.2022.102841.

[105] J. Oliva, J. Sanchez, S.R. Servin, J.A. Ruiz-Santoyo, C.R. Garcia, M.A. Vallejo, L. Álvarez-Valtierra, C. Gomez-Solis, Enhancing the photocatalytic degradation of ciprofloxacin contaminant using a combined laser irradiation (285/365 nm) and porous g-C_3N_4, Mater Chem Phys 252 (2020) 123198, https://doi.org/10.1016/J.MATCHEMPHYS.2020.123198.

[106] E.M. Rodríguez, G. Márquez, M. Tena, P.M. Álvarez, F.J. Beltrán, Determination of main species involved in the first steps of TiO_2 photocatalytic degradation of organics with the use of scavengers: The case of ofloxacin, Appl Catal B 178 (2015) 44–53, https://doi.org/10.1016/j.apcatb.2014.11.002.

[107] M. Pelaez, P. Falaras, V. Likodimos, K. O'Shea, A.A. de la Cruz, P.S.M. Dunlop, J. A. Byrne, D.D. Dionysiou, Use of selected scavengers for the determination of NF-TiO_2 reactive oxygen species during the degradation of microcystin-LR under visible light irradiation, J Mol Catal A Chem 425 (2016) 183–189, https://doi.org/10.1016/j.molcata.2016.09.035.

[108] B.H.J. Bielski, D.E. Cabelli, R.L. Arudi, A.B. Ross, Reactivity of HO_2/O_2^- radicals in aqueous solution, J Phys Chem Ref Data 14 (1985) 1041–1100, https://doi.org/10.1063/1.555739.

[109] M. Zhu, J. Lu, Y. Hu, Y. Liu, S. Hu, C. Zhu, Photochemical reactions between 1,4-benzoquinone and O2•−, Environ. Sci. Pollut. Res. 27 (2020) 31289–31299, https://doi.org/10.1007/S11356-020-09422-8.

[110] M. Nien Schuchmann, E. Bothe, J. von Sonntag, C. von Sonntag, Reaction of OH radicals with benzoquinone in aqueous solutions. A pulse radiolysis study, J. Chem. Soc. Perkin Trans. 2 (1998) 791–796, https://doi.org/10.1039/A708772A.

[111] K.C. Kurien, P.A. Robins, Photolysis of aqueous solutions of p-benzoquinone: a spectrophotometric investigation, J. Chem. Soc. B (1970) 855–859, https://doi.org/10.1039/J29700000855.

[112] J.T. Schneider, D.S. Firak, R.R. Ribeiro, P. Peralta-Zamora, Use of scavenger agents in heterogeneous photocatalysis: truths, half-truths, and misinterpretations, PCCP 22 (2020) 15723–15733, https://doi.org/10.1039/d0cp02411b.

[113] A.I. Ononye, A.R. McIntosh, J.R. Bolton, Mechanism of the photochemistry of p-benzoquinone in aqueous solutions. 1. Spin trapping and flash photolysis electron paramagnetic resonance studies, J. Phys. Chem. 90 (1986) 6266–6270, https://doi.org/10.1021/J100281A039.

[114] C.L. Greenstock, R.W. Miller, The oxidation of tiron by superoxide anion. Kinetics of the Reaction in Aqueous Solution and in Chloroplasts, Biochim Biophys Acta 396 (1975) 11–16, https://doi.org/10.1016/0005-2728(75)90184-X.

[115] W. Bors, M. Saran, C. Michel, Pulse-radiolytic investigations of catechols and catecholamines II. Reactions of tiron with oxygen radical species, BBA - General Subjects 582 (1979) 537–542, https://doi.org/10.1016/0304-4165(79)90145-4.

[116] M.S. Alam, B.S.M. Rao, E. Janata, ·OH reactions with aliphatic alcohols: evaluation of kinetics by direct optical absorption measurement, A Pulse Radiolysis Study, Radiation Physics and Chemistry 67 (2003) 723–728, https://doi.org/10.1016/S0969-806X(03)00310-4.

[117] W.H.M. Abdelraheem, M.K. Patil, M.N. Nadagouda, D.D. Dionysiou, Hydrothermal synthesis of photoactive nitrogen- and boron- codoped TiO_2

nanoparticles for the treatment of bisphenol A in wastewater: Synthesis, photocatalytic activity, degradation byproducts and reaction pathways, Appl Catal B 241 (2019) 598–611, https://doi.org/10.1016/J.APCATB.2018.09.039.
[118] S. Gligorovski, R. Strekowski, S. Barbati, D. Vione, Environmental implications of hydroxyl radicals (•OH), Chem Rev 115 (2015) 13051–13092, https://doi.org/10.1021/CR500310B.
[119] M. Sahni, B.R. Locke, Quantification of hydroxyl radicals produced in aqueous phase pulsed electrical discharge reactors, Ind Eng Chem Res 45 (2006) 5819–5825, https://doi.org/10.1021/IE0601504.
[120] L.L.S. Silva, W. Abdelraheem, M.N. Nadagouda, A.M. Rocco, D.D. Dionysiou, F. V. Fonseca, C.P. Borges, Novel microwave-driven synthesis of hydrophilic polyvinylidene fluoride/polyacrylic acid (PVDF/PAA) membranes and decoration with nano zero-valent-iron (nZVI) for water treatment applications, J Memb Sci 620 (2021) 118817, https://doi.org/10.1016/J.MEMSCI.2020.118817.
[121] L. Wang, B. Li, D.D. Dionysiou, B. Chen, J. Yang, J. Li, Overlooked formation of H_2O_2 during the hydroxyl radical-scavenging process when using alcohols as scavengers, Environ Sci Technol 56 (2022) 3386–3396, https://doi.org/10.1021/ACS.EST.1C03796.
[122] A. Krishnan, S. Beena, M. Chandran, Fabrication and evaluation of CeO_2-Fe_2O_3 mixed oxide for hydrogen evolution by photo water splitting reaction under visible light irradiation, Mater Today Proc 18 (2019) 4968–4976, https://doi.org/10.1016/J.MATPR.2019.07.489.
[123] B.R. Shah, U.D. Patel, Mechanistic aspects of photocatalytic degradation of Lindane by TiO_2 in the presence of Oxalic acid and EDTA as hole-scavengers, J Environ Chem Eng 9 (2021) 105458, https://doi.org/10.1016/J.JECE.2021.105458.
[124] B.G. Ershov, E. Janata, M.S. Alam, A.V. Gordeev, A pulse radiolysis study of the reactions of the hydrated electron and hydroxyl radical with the oxalate ion in neutral aqueous solution, High Energ. Chem. 42 (2008) 1–6, https://doi.org/10.1134/s0018143908010013.
[125] S.F. Lee, E. Jimenez-Relinque, I. Martinez, M. Castellote, Effects of Mott-Schottky frequency selection and other controlling factors on flat-band potential and band-edge position determination of TiO_2, Catalysts 13 (2023) 1000, https://doi.org/10.3390/CATAL13061000.
[126] N. Sakai, Y. Ebina, K. Takada, T. Sasaki, Electronic band structure of titania semiconductor nanosheets revealed by electrochemical and photoelectrochemical studies, J Am Chem Soc 126 (2004) 5851–5858, https://doi.org/10.1021/JA0394582.
[127] Y. Liu, L. Chen, X. Liu, T. Qian, M. Yao, W. Liu, H. Ji, Tuning band structure of graphitic carbon nitride for efficient degradation of sulfamethazine: Atmospheric condition and theoretical calculation, Chin. Chem. Lett. 33 (2022) 1385–1389, https://doi.org/10.1016/J.CCLET.2021.08.061.
[128] Q. Su, Y. Li, R. Hu, F. Song, S. Liu, C. Guo, S. Zhu, W. Liu, J. Pan, Heterojunction photocatalysts based on 2D materials: the role of configuration, Adv Sustain Syst 4 (2020) 2000130, https://doi.org/10.1002/ADSU.202000130.
[129] P.M. Wood, The potential diagram for oxygen at pH 7, Biochem. J 253 (1988) 287–289, https://doi.org/10.1042/BJ2530287.
[130] K.S. Ranjith, D. Ranjith Kumar, S.M. Ghoreishian, Y.S. Huh, Y.K. Han, R. T. Rajendra Kumar, A radially controlled ZnS interlayer on ultra-long ZnO–Gd_2S_3 core–shell nanorod arrays for promoting the visible photocatalytic degradation of antibiotics, Nanoscale 12 (2020) 14047–14060, https://doi.org/10.1039/D0NR03094E.
[131] W.H. Koppenol, D.M. Stanbury, P.L. Bounds, Electrode potentials of partially reduced oxygen species, from dioxygen to water, Free Radic Biol Med 49 (2010) 317–322, https://doi.org/10.1016/J.FREERADBIOMED.2010.04.011.